

EVIDENCE OF PHOTOSPHERE EMISSION ORIGIN FOR GAMMA-RAY BURST PROMPT EMISSION

YAN-ZHI MENG^{1,2}

¹School of Astronomy and Space Science, Nanjing University, Nanjing 210023, China; yzmeng@nju.edu.cn and

²Key Laboratory of Modern Astronomy and Astrophysics (Nanjing University), Nanjing 210023, Ministry of Education, China

Draft version December 13, 2022

ABSTRACT

The physical origins of gamma-ray burst (GRB) prompt emission (photosphere or synchrotron) are still subject to debate, after more than five decades. Here, we find that many of the observed characteristics of 15 long GRBs, which have the highest prompt emission efficiency ϵ_γ ($\epsilon_\gamma \gtrsim 80\%$), strongly support photosphere (thermal) emission origin, in the following ways: (1) the relation between E_p and E_{iso} is almost $E_p \propto (E_{\text{iso}})^{1/4}$ and the dispersion is quite small; (2) the simple power-law shape of the X-ray afterglow light curves and the presence of significant reverse shock signals in the optical afterglow light curves; (3) the best fits using the cutoff power-law model for the time-integrated spectra; and (4) the consistent efficiency from observations (with E_{iso}/E_k) and the predictions from the photosphere emission model (with η/Γ). We then further investigate the characteristics of the long GRBs for two distinguished samples ($\epsilon_\gamma \gtrsim 50\%$ and $\epsilon_\gamma \lesssim 50\%$). It is found that the different distributions for E_p and E_{iso} , and the similar observed efficiency (from the X-ray afterglow) and theoretically predicted efficiency (from the prompt emission or the optical afterglow), follow the predictions of the photosphere emission model well. Also, based on the same efficiency, we derive an excellent correlation of $\Gamma \propto E_{\text{iso}}^{1/8} E_p^{1/2} / (T_{90})^{1/4}$ to estimate Γ . Finally, we show that different distributions for E_p and E_{iso} , and the consistent efficiency, exist for short GRBs. We also give a natural explanation of the extended emission ($\epsilon_\gamma \lesssim 50\%$) and the main pulse ($\epsilon_\gamma \gtrsim 50\%$).

Subject headings: gamma-ray burst: general – radiation mechanisms: thermal – radiative transfer – scattering

1. INTRODUCTION

More than 50 yr after its discovery, the radiation mechanism of gamma-ray burst (GRB) prompt emission (photosphere emission or synchrotron emission) still remains unidentified (e.g., Mészáros 2002; Zhang & Yan 2011; Uhm & Zhang 2014; Geng et al. 2018, 2019; Lin et al. 2018; Zhang et al. 2018a,b, 2021; Li et al. 2019b, 2021; Burgess et al. 2020; Yang et al. 2020; Zhang 2020; Iyyani & Sharma 2021; Vyas et al. 2021; Zhang et al. 2021b; Vereshchagin et al. 2022). The photospheric emission is the basic prediction of the classical fireball model (Goodman 1986; Paczynski 1986) for a GRB, because the optical depth τ at the jet base is much larger than unity (e.g. Piran 1999). As the fireball expands, the optical depth drops down. The internally trapped thermal photons finally escape at the photosphere ($\tau = 1$). Indeed, based on the spectral analysis, a quasi-thermal component has been found in several *Swift* GRBs (Ryde 2004, 2005; Ryde & Pe’er 2009) and *Fermi* GRBs (Guiriec et al. 2011, 2013; Axelsson et al. 2012; Ghirlanda et al. 2013; Larsson et al. 2015; Tang et al. 2021; Deng et al. 2022; Wang et al. 2022; Zhao et al. 2022), especially in GRB 090902B (Abdo et al. 2009; Ryde et al. 2010; Zhang 2011). But whether the typically observed Band function (a smoothly joint broken power law; Band et al. 1993) or a cutoff power law (CPL) can be explained by the photosphere emission, namely the photospheric emission model, remains unknown (e.g., Abramowicz et al. 1991; Thompson 1994; Mészáros & Rees 2000; Rees & Mészáros 2005; Pe’er & Ryde 2011; Fan et al. 2012; Lazzati et al. 2013; Ruffini et al. 2013; Bégué & Pe’er 2015; Gao et al. 2015; Pe’er et al. 2015; Ryde et al.

2017; Acuner & Ryde 2018; Hou et al. 2018; Meng et al. 2018, 2019, 2022; Li 2019a,c, 2020; Acuner et al. 2020; Dereli-Bégué et al. 2020; Vereshchagin & Siutsou 2020; Wang et al. 2020; Parsotan & Lazzati 2022; Song & Meng 2022). If this scenario is true, the quasi-thermal spectrum should be broadened. Theoretically, two different broadening mechanisms have been proposed (see Appendix A): subphotospheric dissipation (namely, the dissipative photosphere model; Rees & Mészáros 2005; Giannios & Spruit 2007; Vurm & Beloborodov 2016; Beloborodov 2017; Bhattacharya et al. 2018; Bhattacharya & Kumar 2020) or geometric broadening (namely, the probability photosphere model; Pe’er 2008; Pe’er & Ryde 2011; Lundman et al. 2013; Deng & Zhang 2014; Meng et al. 2018, 2019, 2022).

Previously, some of the implications of the statistical properties of the spectral analysis results for a large GRB sample have appeared to support the photosphere emission model. First, lots of bursts have a low-energy spectral index α that is harder than the death line (or the maximum value, $\alpha = -2/3$) of the basic synchrotron model, especially for short GRBs and the peak-flux spectrum (Kaneko et al. 2006; Zhang et al. 2011; Burgess et al. 2017). Second, the spectral width is found to be quite narrow for a significant fraction of GRBs (Axelsson & Borgonovo 2015; Yu et al. 2015). Third, for half or more of GRBs, the CPL is the best-fit empirical model (Goldstein et al. 2012; Gruber et al. 2014; Yu et al. 2016), indicating that the photosphere emission model can naturally interpret their high-energy spectra. Here, we find more convincing evidence for the photosphere emission origin (especially the probability photosphere model) of GRB

prompt emission, by obtaining the prompt efficiency ϵ_γ .

The paper is organized as follows. In Section 2, we state the data accumulation and the scaling relations predicted by the photosphere model. In Section 3, we describe the evidence from long GRBs with extremely high prompt efficiency ϵ_γ ($\epsilon_\gamma \gtrsim 80\%$). Then, in Section 4, the evidence from long GRBs with $\epsilon_\gamma \gtrsim 50\%$ and $\epsilon_\gamma \lesssim 50\%$ is shown. In Section 5, we illustrate the evidence from short GRBs. A brief summary is provided in Section 6.

2. DATA ACCUMULATION AND THE SCALING RELATIONS EXPECTED BY THE FIREBALL MODEL

2.1. Data Accumulation

Generally, the radiation efficiency of the prompt emission ϵ_γ is defined as $E_\gamma/(E_\gamma + E_k)$. Here, E_γ is the radiated energy in the prompt phase and E_k is the remaining kinetic energy in the afterglow phase.

To obtain ϵ_γ , the isotropic energy E_{iso} (namely E_γ) and the $L_{X,11\text{h}}$ (the late-time X-ray afterglow luminosity at 11 hr) data should be accumulated for the GRB sample with the redshift z^1 . Because that, $L_{X,11\text{h}}$ is roughly proportional to the E_k (see Appendix B.1).

(1) For 46 long bursts before GRB 110213A, we use the $L_{X,11\text{h}}$ data given in D’Avanzo et al. (2012). Also, E_{iso} , the isotropic luminosity L_{iso} , the peak spectral energy in the rest frame $E_{p,z}$ (or E_p), the low-energy spectral index α , and the high-energy spectral index β are taken from Nava et al. (2012).

(2) For 117 long bursts after GRB 110213A (see Tables 1–3, with $\epsilon_\gamma \gtrsim 80\%$, $\epsilon_\gamma \lesssim 50\%$, and $\epsilon_\gamma \gtrsim 50\%$, respectively), we calculate the $L_{X,11\text{h}}$ following the method (see Appendix B.1) in D’Avanzo et al. (2012). E_{iso} , L_{iso} , $E_{p,z}$, $T_{90,i}$ (the intrinsic duration in the rest frame, or T_{90}), and z are mainly taken from Minaev & Pozanenko (2020) and Xue et al. (2019).

Our spectral fitting results for the $\epsilon_\gamma \gtrsim 80\%$ sample are given in Table 4. And for several bursts of the $\epsilon_\gamma \lesssim 50\%$ sample, the perfectly consistent observed efficiency (with E_{iso}/E_k) and the theoretically predicted efficiency of the photosphere model (from the prompt emission) are given in Table 5.

In Table 6, for the long-GRB sample with the detection of the peak time of the early optical afterglow (namely T_p or $T_{p,op}$), to obtain the Lorentz factor of the outflow Γ and then $(R_{\text{ph}}/R_s)^{-2/3}$ in Ghirlanda et al. (2018), the consistent predicted efficiency (from the prompt emission and the optical afterglow) of the photosphere model is provided. Also, E_{iso} , L_{iso} , and $E_{p,z}$ are taken from Ghirlanda et al. (2018). In Table 7, its subsample (9 bursts) with the maximum Γ (for fixed L_{iso} ; according to the photosphere model, $\epsilon_\gamma = 50\%$) is provided.

In Table 8, the short-GRB sample (with $L_{X,11\text{h}}$ derived in this work) is given, along with that possessing extended emission. E_{iso} and $E_{p,z}$ are taken from Minaev & Pozanenko (2020).

E_{iso} is generally estimated by $E_{\text{iso}} = 4\pi D_L^2 S_\gamma / (1+z)$, where S_γ is the time-integral fluence in the $1 - 10^4$ keV energy range in the rest frame (in units of erg cm^{-2}) and D_L is the luminosity distance. L_{iso} is estimated as

$L_{\text{iso}} = 4\pi D_L^2 F_p$, where F_p is the peak flux (in units of $\text{erg cm}^{-2} \text{s}^{-1}$). $T_{90,i}$ is calculated as $T_{90,i} = T_{90,ob}/(1+z)$, where $T_{90,ob}$ is determined by the time range between the epochs when the accumulated net photon counts reach the 5% level and the 95% level. And $E_p = (1+z) \cdot E_{p,ob}$, where $E_{p,ob}$ is determined by the peak energy in the νF_ν spectrum.

Typically, the afterglow peak time T_p is estimated from the optical afterglow peak time $T_{p,op}$, since the early X-ray afterglow peak can be produced by “internal” mechanisms (such as the prolonged central engine activity) or bright flares. Also, the bursts with an early multi-peaked optical light curve or an optical peak preceded by a decreasing light curve should be excluded (see Ghirlanda et al. 2018).

2.2. Scaling Relations Predicted by the Photosphere Model

For the photosphere emission model, $\epsilon_\gamma \gtrsim 50\%$ and $\epsilon_\gamma \lesssim 50\%$ should correspond to the unsaturated acceleration case ($\Gamma \lesssim \eta$; $R_{\text{ph}} < R_s$; $E_{\text{iso}}/E_k = \eta Mc^2 / \Gamma Mc^2 = \eta/\Gamma \gtrsim 1$) and the saturated acceleration case ($\Gamma = \eta$; $R_{\text{ph}} > R_s$; $E_{\text{iso}}/E_k = [\eta Mc^2 (R_{\text{ph}}/R_s)^{-2/3}] / \Gamma Mc^2 = (R_{\text{ph}}/R_s)^{-2/3} \lesssim 1$), respectively.

2.2.1. $E_{\text{iso}}/E_k = \eta/\Gamma$ for the unsaturated acceleration case, corresponding to $\epsilon_\gamma \gtrsim 50\%$

When the outflow Lorentz factor Γ at the photosphere radius R_{ph} is less than the baryon loading η ($\eta = E/Mc^2$, where E and M are the injected energy and the baryon mass at the outflow base, respectively), the photosphere emission is in the unsaturated acceleration case (or $R_{\text{ph}} < R_s$; where $R_s = \eta r_0$, and r_0 is the initial acceleration radius). In this case, $\Gamma = R_{\text{ph}}/r_0$.

For the unsaturated acceleration case, the observed temperature $T_{\text{ob}} = D \cdot T_{\text{comoving}} = \Gamma \cdot (T_0/\Gamma) = T_0$. Here, D is the Doppler factor, T_{comoving} is the photon temperature in the outflow comoving frame, and T_0 is the temperature at the outflow base r_0 . Thus, $E_{\text{iso}} = E = \eta Mc^2$. Also, because all the thermal energy is released at the photosphere radius (where there is no remaining energy to accelerate the jet), the Lorentz factor in the afterglow phase will remain as Γ , namely $E_k = \Gamma Mc^2$. So we should have $E_{\text{iso}}/E_k = \eta Mc^2 / \Gamma Mc^2 = \eta/\Gamma \gtrsim 1$ (see Figure 1(b) and 2(e)), corresponding to $\epsilon_\gamma \gtrsim 50\%$.

2.2.2. $E_p \propto (E_{\text{iso}})^{1/4}$ for $\epsilon_\gamma \gtrsim 50\%$

For the photosphere emission model, the peak energy of the observed spectrum E_p corresponds to the temperature of the observed blackbody T_{ob} . In the unsaturated regime ($R_{\text{ph}} < R_s$, $\epsilon_\gamma \gtrsim 50\%$), $T_{\text{ob}} = T_0$. Since $T_0 \propto E^{1/4} \propto (E_{\text{iso}})^{1/4}$, we should have $E_p \propto (E_{\text{iso}})^{1/4}$ (see Figures 3–5; for $\epsilon_\gamma \gtrsim 80\%$ and $\epsilon_\gamma \gtrsim 50\%$ of long GRBs, and short GRBs).

2.2.3. For $\epsilon_\gamma \lesssim 50\%$, $E_{\text{iso}} = E \cdot (R_{\text{ph}}/R_s)^{-2/3}$ and $E_p \propto E^{1/4} \cdot (R_{\text{ph}}/R_s)^{-2/3}$

For $\epsilon_\gamma \lesssim 50\%$ ($R_{\text{ph}} > R_s$), the outflow performs adiabatic expansion at $r > R_s$. Thus, the comoving temperature decreased as $T_{\text{comoving}} = (T_0/\Gamma) \cdot (r/R_s)^{-2/3}$. The escaped photons at R_{ph} have $E_{\text{iso}} = E \cdot (R_{\text{ph}}/R_s)^{-2/3}$

¹ The redshift data are publicly available at <http://www.mpe.mpg.de/jcg/grbgen.html>.

TABLE 1
THE OBSERVED QUANTITIES FOR THE BURSTS WITH EXTREMELY HIGH EFFICIENCY ($\epsilon_\gamma \gtrsim 80\%$).

| GRB | z | L_{iso} (10^{52} erg s $^{-1}$) | E_{iso} (10^{52} erg) | $L_{X,11}$ (10^{45} erg s $^{-1}$) | Efficiency | $E_{p,z}$ (keV) | α | β | best-fitted model |
|------------------------|--------|---|--------------------------------------|---|---------------------------|-----------------------|------------------|--------------------|----------------------|
| 990705 ^a | 0.8424 | 1.61 ± 0.15^c | 21.8 ± 0.8 | 1.14 | 0.83 (0.99 ^f) | 551 ± 17 | -0.72 ± 0.03 | -2.68 ± 0.15^e | |
| 000210 ^a | 0.8463 | 9.76 ± 0.5^c | 19.3 ± 0.5 | 1.67 | 0.74 (0.97 ^f) | 687^{+39}_{-37} | | | |
| 060927 ^b | 5.47 | 10.8 ± 0.8 | 7.56 ± 0.46 | 0.28 | 0.96 | 459 ± 90 | -0.81 ± 0.36 | | |
| 061007 ^b | 1.261 | 10.9 ± 0.9 | 101 ± 1.4 | 1.11 | 0.97 | 965 ± 27 | -0.75 ± 0.02 | -2.79 ± 0.09 | |
| 080319B ^b | 0.9382 | 10.2 ± 0.9 | 142 ± 3 | 3.90 | 0.91 | 1307 ± 43 | -0.86 ± 0.01 | -3.59 ± 0.45 | |
| 080607 ^b | 3.0363 | 225.9 ± 45.3 | 186 ± 10 | 3.46 | 0.97 | 1691 ± 169 | -1.08 ± 0.06 | | |
| 081203A ^b | 2.05 | 2.82 ± 0.19 | 35.0 ± 12.8 | 1.52 | 0.90 | 1541 ± 756 | -1.29 ± 0.14 | | |
| 110205A ^b | 2.22 | 2.51 ± 0.34 | 55.9 ± 5.3 | 2.12 | 0.92 | 715 ± 238 | -1.52 ± 0.14 | | |
| 110818A ^c | 3.36 | 6.76 ± 0.76 | 21.7 ± 1.02 | 0.99 | 0.93 | 799.45 ± 371.90 | -1.19 ± 0.08 | | CPL ^d |
| 120729A ^a | 0.80 | | 2.3 ± 1.5 | 0.034 | 0.94 | 559 ± 57 | | | |
| 130606A ^a | 5.913 | | 28.3 ± 5.2 | 1.26 | 0.95 | 2032^{+622}_{-346} | -1.14 ± 0.15 | | CPL ^e |
| 131108A ^a | 2.40 | 26.22 ± 0.6^c | 54 ± 2.4 | 1.98 | 0.93 | 1217^{+105}_{-88} | -1.16 ± 0.07 | | CPL ^e |
| 150821A ^a | 0.755 | 0.77 ± 0.03^c | 15.5 ± 1.2 | 1.05 | 0.78 | 765^{+188}_{-126} | -1.52 ± 0.05 | | CPL ^e |
| 160410A ^{a,s} | 1.717 | | 9.3 ± 1.8 | 0.44 | 0.89 | 3853^{+1429}_{-973} | -0.71 ± 0.20 | | CPL ^e |
| 161014A ^c | 2.823 | 5.21 ± 0.52 | 9.49 ± 0.50 | 0.55 | 0.90 | 646.18 ± 55.13 | -0.76 ± 0.08 | | CPL ^d |
| 170214A ^a | 2.53 | 30.32 ± 0.85^c | 318.43 ± 0.21 | 1.94 | 0.99 | 1810 ± 34 | -0.98 ± 0.01 | -2.51 ± 0.10^d | |
| 130606A ^a | 5.913 | | 28.3 ± 5.2 | 1.26 | 0.95 | 2032^{+622}_{-346} | -1.14 ± 0.15 | | CPL ^e |

^a E_{iso} and $E_{p,z}$ are taken from Minaev & Pozanenko (2020). ^b E_{iso} , $E_{p,z}$, L_{iso} , α and β are taken from Nava et al. (2012). ^c E_{iso} , $E_{p,z}$ and L_{iso} (or L_{iso} alone) are taken from Xue et al. (2019). ^d The spectral analysis results are from the Fermi GBM Burst Catalog (von Kienlin et al. 2020). ^e The spectral analysis results are from the Konus/Wind Burst Catalog (Tsvetkova et al. 2017). ^f The extremely high efficiency claimed in Lloyd-Ronning & Zhang (2004). ^s The short GRB.

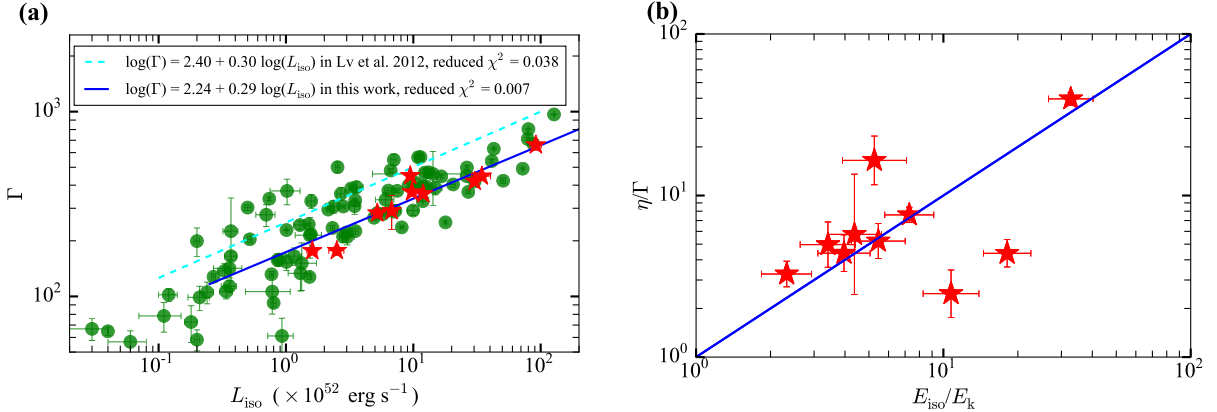


FIG. 1.— The $L_{\text{iso}} - \Gamma$ correlation and the $E_{\text{iso}}/E_k - \eta/\Gamma$ correlation for the selected extremely high-efficiency GRBs. (a) The correlation of L_{iso} and Γ . Obviously, the tight correlation of $\Gamma \propto (L_{\text{iso}})^{0.29}$ (the red stars, reduced $\chi^2 = 0.007$) is found, which is well consistent with the prediction of the neutrino annihilation from the hyperaccretion disk, $\Gamma \propto (L_{\text{iso}})^{7/27} = (L_{\text{iso}})^{0.26}$. Thus, the jet is likely to be thermal-dominated. The cyan dashed line shows the $L_{\text{iso}} - \Gamma$ correlation found in Lü et al. (2012) (reduced $\chi^2 = 0.038$, for the large Γ sample of green circles (Xue et al. 2019)). (b) The correlation of E_{iso}/E_k and η/Γ . A significant linear correlation is found, and they are almost the same when we take $E_{k,52} = 5 * L_{X,45}$ (reduced $\chi^2 = 0.138$). This is well consistent with the predicted $E_{\text{iso}}/E_k = \eta Mc^2 / \Gamma Mc^2 = \eta/\Gamma$ by the photosphere emission model in the unsaturated acceleration regime.

and $E_p = 2.7kT_0 \cdot (R_{\text{ph}}/R_s)^{-2/3} \propto E^{1/4} \cdot (R_{\text{ph}}/R_s)^{-2/3}$. So, E_{iso} and E_p should both decrease by the same factor of $(R_{\text{ph}}/R_s)^{-2/3}$, compared with the $E_p \propto (E_{\text{iso}})^{1/4}$ correlation for $\epsilon_\gamma \gtrsim 50\%$ (see Figures 4 and 5).

$$2.2.4. \text{ For } \epsilon_\gamma \lesssim 50\%, E_{\text{iso}}/E_k = (R_{\text{ph}}/R_s)^{-2/3} = \frac{1}{[(E_p/2.7k)^4 * (4\pi r_1^2 ac)/E_{\text{iso}}]^{1/3}}$$

For the $\epsilon_\gamma \lesssim 50\%$ sample (saturated acceleration, $E_k = E$), we should have

$$E_{\text{iso}} = E \cdot (R_{\text{ph}}/R_s)^{-2/3} \quad (1)$$

and

$$\begin{aligned} E_p &= 2.7kT_0 \cdot (R_{\text{ph}}/R_s)^{-2/3} \\ &= 2.7k(L/4\pi r_0^2 ac)^{1/4} \cdot (R_{\text{ph}}/R_s)^{-2/3} \\ &= 2.7k(E/4\pi r_1^2 ac)^{1/4} \cdot (R_{\text{ph}}/R_s)^{-2/3} \\ &= 2.7k(4\pi r_1^2 ac)^{-1/4} \cdot E^{1/4} \cdot (R_{\text{ph}}/R_s)^{-2/3}, \quad (2) \end{aligned}$$

here $r_1^2 \simeq r_0^2 * T_{90}$. From the relation of $\log(E_p) = 2.54 + 0.25 \log(E_{\text{iso}})$ in Figure 3(b), we obtain $r_1 = 8.45 \times 10^8$ cm. Then, from Equation (1) and Equation (2), we get

$$(E_p)^4/E_{\text{iso}} = (2.7k)^4 * (4\pi r_1^2 ac)^{-1} \cdot (R_{\text{ph}}/R_s)^{-2}, \quad (3)$$

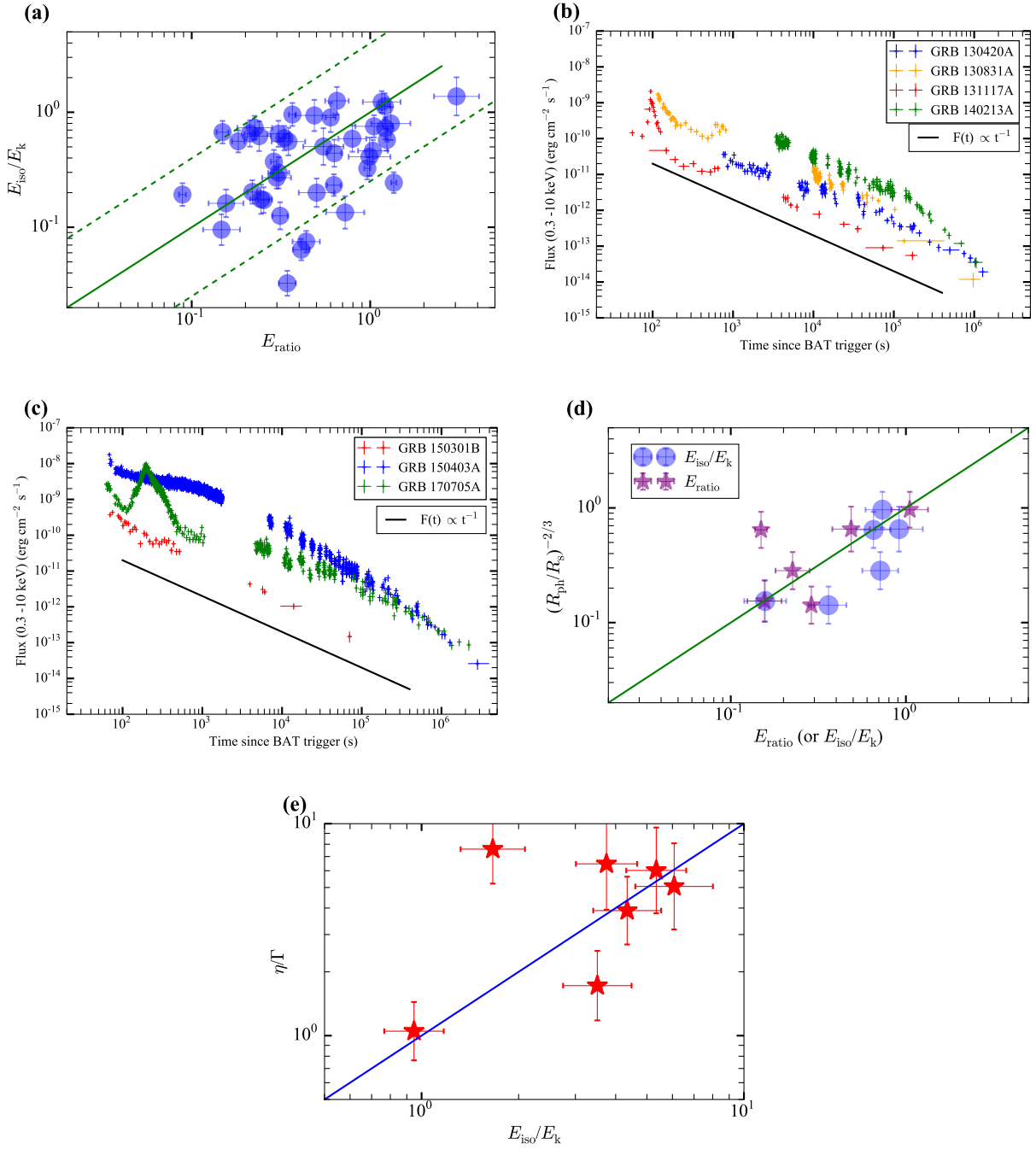


FIG. 2.— The similar observed efficiency (with E_{iso}/E_k from the X-ray afterglow) and theoretically predicted efficiency (from the photosphere emission model for the bursts after GRB 110213A). (a) The distribution of E_{ratio} ($E_{\text{ratio}} = [(E_p/2.7k)^4 * (4\pi r_s^2 ac)/E_{\text{iso}}]^{1/3}$, from the prompt emission) and E_{iso}/E_k for the $\epsilon_\gamma \lesssim 50\%$ sample (see Table 2). They are found to be well centered around the equal-value line, and have a linear correlation (reduced $\chi^2 = 0.172$). The dispersion is likely to be caused by the estimation error for E_k , since many X-ray afterglow light curves are not the power law with a slope of -1 . (b) and (c) The X-ray afterglow light curves for the bursts (7 bursts) with almost same E_{ratio} and E_{iso}/E_k (see Table 5). We find all these light curves do have the power-law shape with a slope of ~ -1 . (d) The distribution of E_{ratio} , E_{iso}/E_k and $(R_{\text{ph}}/R_s)^{-2/3}$ for the sample (6 bursts, see Table 2) with detections of peak time of the optical afterglow (to estimate the Γ and thus $(R_{\text{ph}}/R_s)^{-2/3}$). It is found that 1 burst has the almost same values for these three quantities and the other 5 bursts have the almost same values for two quantities of them (reduced $\chi^2 = 0.089$ for all 12 markers). (e) The consistent efficiency from observation (with E_{iso}/E_k) and the prediction of photosphere emission model (with η/Γ) for the $\epsilon_\gamma \gtrsim 50\%$ sample with detections of peak time of the optical afterglow (7 bursts, see Table 3; reduced $\chi^2 = 0.120$).

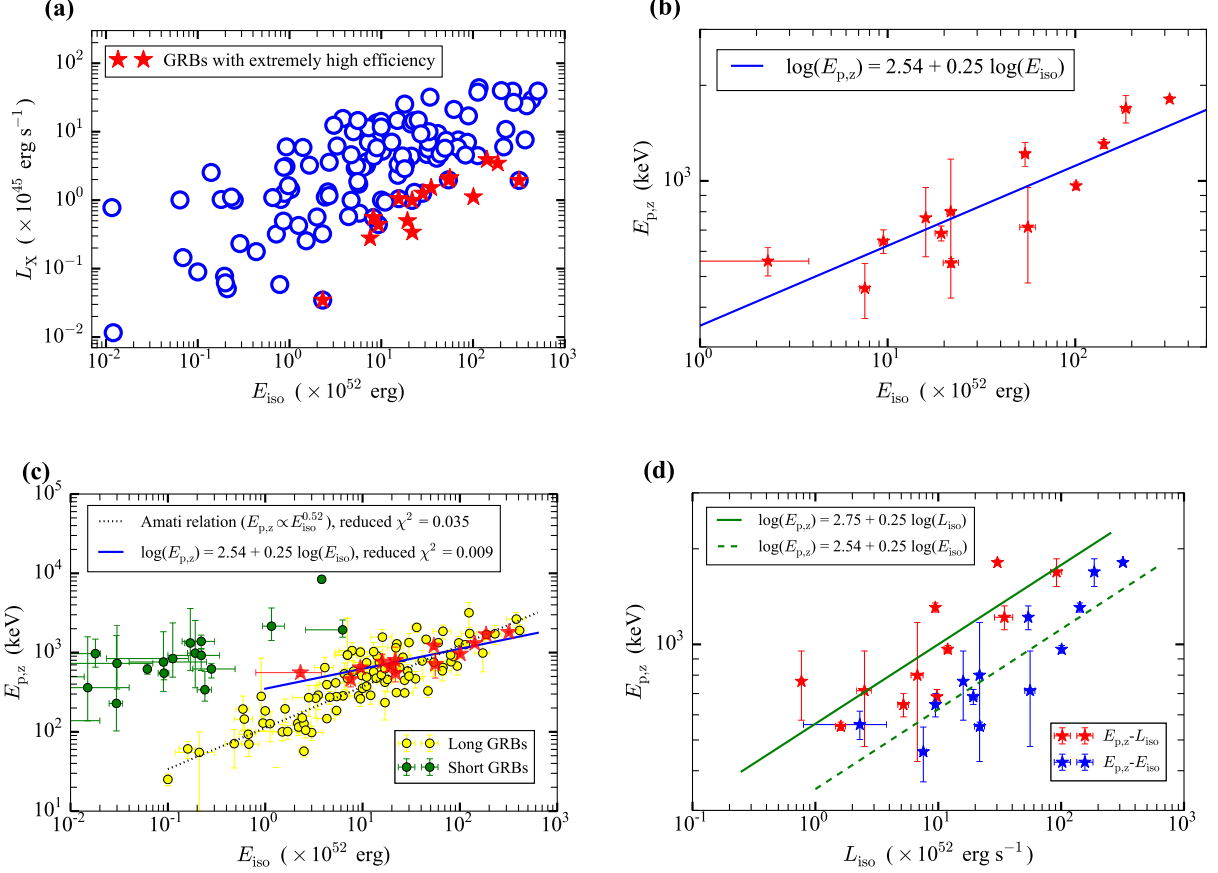


FIG. 3.— The $E_p \propto (E_{\text{iso}})^{1/4}$ and $E_p \propto (L_{\text{iso}})^{1/4}$ relations for the GRBs with the highest prompt efficiency ϵ_γ ($\epsilon_\gamma \gtrsim 80\%$; see Table 1). (a) The E_{iso} and calculated $L_{X,11\text{h}}$ (the late-time X-ray afterglow luminosity at 11 hours) distribution for the whole GRB sample used (117 bursts, after GRB 110213A) with redshift. The red stars with the smallest $L_{X,11\text{h}}$ represent the bursts with the highest prompt efficiency. (b) The E_p and E_{iso} distribution for the selected 15 long GRBs. The best-fit result is $\log(E_p) = 2.54 + 0.25 \log(E_{\text{iso}})$, quite consistent with the $E_p \propto (E_{\text{iso}})^{1/4}$ relation predicted by the photosphere (thermal) emission model. (c) Comparison of the E_p and E_{iso} distributions for the selected GRBs (red stars) and the large sample of long GRBs (see Figure 3 in Zhang et al. (2018b)) (yellow circles). Obviously, the dispersion for the selected GRBs is quite small (reduced $\chi^2 = 0.009$) relative to that for the large sample (reduced $\chi^2 = 0.035$). The black dotted line shows the Amati relation (Amati et al. 2002) for the large sample. (d) Comparison of the $E_p - E_{\text{iso}}$ distribution (red stars) and the $E_p - L_{\text{iso}}$ distribution (blue stars) for the selected GRBs. Likewise, the $E_p \propto (L_{\text{iso}})^{1/4}$ relation exists. The best-fit result is $\log(E_p) = 2.75 + 0.23 \log(L_{\text{iso}})$. And the dispersion (reduced $\chi^2 = 0.012$) is found to be similar to that of $E_p \propto (E_{\text{iso}})^{1/4}$.

thus

$$(R_{\text{ph}}/R_s)^{-2/3} = [(E_p/2.7k)^4 * (4\pi r_1^2 ac)/E_{\text{iso}}]^{1/3}. \quad (4)$$

Combined with the abovementioned $E_{\text{iso}}/E_k = (R_{\text{ph}}/R_s)^{-2/3}$, $E_{\text{ratio}} = E_{\text{iso}}/E_k = (R_{\text{ph}}/R_s)^{-2/3}$ is predicted ($E_{\text{ratio}} = [(E_p/2.7k)^4 * (4\pi r_1^2 ac)/E_{\text{iso}}]^{1/3}$; see Figures 2, and 5–7).

2.2.5. $\Gamma \propto E_{\text{iso}}^{1/8} E_p^{1/2}/(T_{90})^{1/4}$ correlation

As in the previous statement and shown in Figure 7(b), for $\epsilon_\gamma \lesssim 50\%$, we have $E_{\text{ratio}} = (R_{\text{ph}}/R_s)^{-2/3}$. Considering

$$R_{\text{ph}} = \frac{\sigma_T}{8\pi m_p c^3} \frac{L}{\Gamma^3}, \quad (5)$$

and $R_s = \Gamma \cdot r_0$, we have

$$[(E_p/2.7k)^4 * (4\pi r_1^2 ac)/E_{\text{iso}}]^{1/3} = \left(\frac{\sigma_T}{8\pi m_p c^3} \frac{E_{\text{iso}}/T_{90}}{\Gamma^4 \cdot r_0} \right)^{-2/3}. \quad (6)$$

Thus, we can use the quantities of the prompt emission (E_{iso} , E_p and T_{90}) to estimate the Lorentz factor Γ , just as the obtained $\Gamma = 10^{3.33} L_{\text{iso}}^{0.46} E_p^{-0.43}$ from the statistic fitting in Liang et al. (2015) (see Figures 7(c) and 8). Based on Equation (6), we derive

$$\Gamma \propto E_{\text{iso}}^{1/8} E_p^{1/2}/(T_{90})^{1/4}. \quad (7)$$

Considering the constants, we obtain

$$\Gamma = 19.67 \cdot E_{\text{iso}}^{1/8} E_p^{1/2}/(T_{90})^{1/4}. \quad (8)$$

For the $\epsilon_\gamma \gtrsim 50\%$ case, from

$$R_{\text{ph}} = \left[\frac{\sigma_T}{6m_p c} \frac{L_{\text{iso}}}{4\pi c^2 \eta} r_0^2 \right]^{1/3}, \quad (9)$$

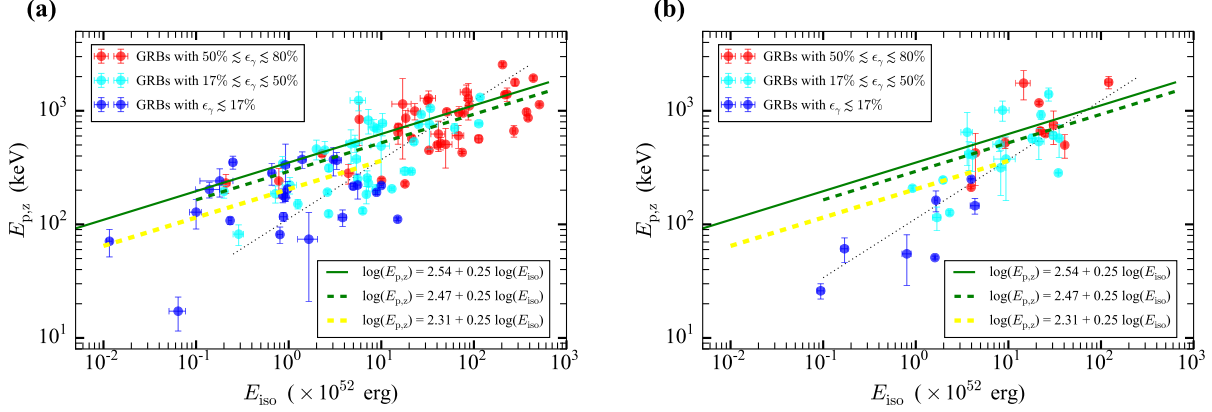


FIG. 4.— The different distributions for E_p and E_{iso} of the two distinguished samples ($\epsilon_\gamma \gtrsim 50\%$ and $\epsilon_\gamma \lesssim 50\%$; see Tables 2 and 3) for the long GRBs. (a) The E_p and E_{iso} distribution for the bursts after GRB 110213A (117 bursts, with $L_{X,11h}$ derived in this work). For the $\epsilon_\gamma \gtrsim 50\%$ (red circles) sample, the best-fit result is $\log(E_p) = 2.47 + 0.25 \log(E_{\text{iso}})$ (reduced $\chi^2 = 0.039$; for the black dotted line of the typical Amati relation, reduced $\chi^2 = 0.079$), well consistent with the predicted $E_p \propto (E_{\text{iso}})^{1/4}$ by the photosphere emission model. For the $\epsilon_\gamma \lesssim 50\%$ (blue and cyan circles) sample, the up-most distribution is found well around $\log(E_p) = 2.54 + 0.25 \log(E_{\text{iso}})$, and the best-fit result is $\log(E_p) = 2.31 + 0.26 \log(E_{\text{iso}})$ (reduced $\chi^2 = 0.076$; for the typical Amati relation, reduced $\chi^2 = 0.113$), quite below that. (b) The E_p and E_{iso} distribution for the bursts before GRB 110213A (46 bursts, with $L_{X,11h}$ given in D’Avanzo et al. 2012). The different distributions for E_p and E_{iso} of the two distinguished samples ($\epsilon_\gamma \gtrsim 50\%$ and $\epsilon_\gamma \lesssim 50\%$) are also found, similar to the distributions for the bursts after GRB 110213A.

we have

$$\begin{aligned} \Gamma &= R_{\text{ph}}/r_0 = \left[\frac{\sigma_T}{6m_p c} \frac{L_{\text{iso}}}{4\pi c^2 \eta} r_0^2 \right]^{1/3} / r_0 \\ &= \left[\frac{\sigma_T}{6m_p c} \frac{L_{\text{iso}}}{4\pi c^2 \eta r_0} \right]^{1/3}. \end{aligned} \quad (10)$$

Thus, $L_{\text{iso}} \propto E_{\text{iso}}/(T_{90}) \propto \eta \cdot \Gamma^3$. Combined with $E_{\text{iso}}/E_k = \eta M c^2 / \Gamma M c^2 = \eta / \Gamma$, we have $1/T_{90} \propto (1/E_k) \cdot \Gamma^4$, namely $E_k \propto \Gamma^4 \cdot T_{90}$. Putting this into $\Gamma \propto (E_k)^{1/8} \cdot [T_p/(1+z)]^{-3/8}$, we obtain $\Gamma \propto \Gamma^{1/2} \cdot (T_{90})^{1/8} \cdot [T_p/(1+z)]^{-3/8}$, namely $\Gamma^{1/2} \cdot (T_{90})^{-1/8} \propto [T_p/(1+z)]^{-3/8}$. From Figure 9(a) (discussed in Section 2.2.7), we have $\Gamma \propto E_p/(T_{90})^{1/4}$. So, as in the $\epsilon_\gamma \lesssim 50\%$ case, $E_p^{1/2}/(T_{90})^{1/4} \propto [T_p/(1+z)]^{-3/8}$ is obtained (as discussed in Section 2.2.6). This means that the Equation (7) is also available for the $\epsilon_\gamma \gtrsim 50\%$ case. After considering the constants, we get

$$\Gamma = 16.75 \cdot E_{\text{iso}}^{1/8} E_p^{1/2} / (T_{90})^{1/4}. \quad (11)$$

Note that different constants for the $\epsilon_\gamma \lesssim 50\%$ case and the $\epsilon_\gamma \gtrsim 50\%$ case are predicted (see Figure 7(d) and (e)). Also, the calculation of Γ in Figure 9(a), using the optical afterglow, has assumed an efficiency of $\sim 20\%$ (namely, $E_k = 5 \cdot E_{\text{iso}}$). In fact, when calculating Γ , we should modify E_k based on the real efficiency (η/Γ). For the $\epsilon_\gamma \gtrsim 50\%$ case, we typically have $\eta/\Gamma \sim 3.5$ (see Figure 9(a) and Figure 10). Thus, the constant ~ 16.75 should be ~ 1.4 times smaller.

2.2.6. $T_p/(1+z) \propto [E_p/(T_{90})^{1/2}]^{-4/3}$ correlation

Note that when using the optical afterglow (the peak time T_p) to obtain Γ , we have

$$\begin{aligned} \Gamma &\propto (E_k)^{1/8} \cdot [T_p/(1+z)]^{-3/8} \\ &\propto (E_{\text{iso}}/\epsilon_\gamma)^{1/8} \cdot [T_p/(1+z)]^{-3/8}, \end{aligned} \quad (12)$$

where ϵ_γ is normally taken as 0.2. Then, if the Equation (7) is correct, combining Equation (7) and Equation (12) should give (see Figure 7(d))

$$T_p/(1+z) \propto [E_p/(T_{90})^{1/2}]^{-4/3}. \quad (13)$$

2.2.7. $\Gamma \propto E_p/(T_{90})^{1/4}$ correlation

As shown in Figure 4(a), we have $E_p \propto (E_{\text{iso}})^{1/4}$ for both the $\epsilon_\gamma \gtrsim 50\%$ case (smaller dispersion) and the $\epsilon_\gamma \lesssim 50\%$ case (larger dispersion). Then, with the Equation (7), we should obtain $\Gamma \propto E_p/(T_{90})^{1/4}$. On the other hand, from Figure 1(a) and Figure 11(a) we have approximately $\Gamma \propto (L_{\text{iso}})^{1/4}$, thus $\Gamma \propto E_p/(T_{90})^{1/4}$ is also likely to be obtained (see Figure 9).

2.3. Tightness of the Scaling Relations and Data Errors

To quantitatively measure the tightness of the scaling relations, we calculate the statistical value

$$\chi^2 = \sum_{i=1}^N (\lg y_i - a \lg x_i - b)^2, \quad (14)$$

for each relation of $\lg y = a \lg x - b$ (for example, $\lg E_p = 0.25 \lg E_{\text{iso}} + 2.54$). The reduced $\chi^2 = \chi^2/\text{degrees of freedom}$ (dof = $N - 2$) for each relation is given in the caption for the corresponding figure. Note that $\sqrt{\chi^2/\text{dof}}$ is approximate to the typical dispersion measure σ (both in units of dex). In Figure 10, for the Gaussian fit, $\chi^2 = \sum (y_i - \bar{y}_{i,\text{model}})^2$ is adopted.

To show how well the data follows the predicted relations, the missing errors for the considered quantities are estimated. For the compound quantities (such as E_{iso}/E_k), the errors are estimated by error propagation: $\Delta[\lg(E_{\text{iso}}/E_k)] = \Delta[\lg(E_{\text{iso}}) - \lg(E_k)] = \Delta[\lg(E_{\text{iso}})] + \Delta[\lg(E_k)]$. For the $L_{X,11h}$ derived in this work, $T_{p,op}$, and $T_{90,i}$, the errors at the 90% confidence level (~ 0.1 dex)

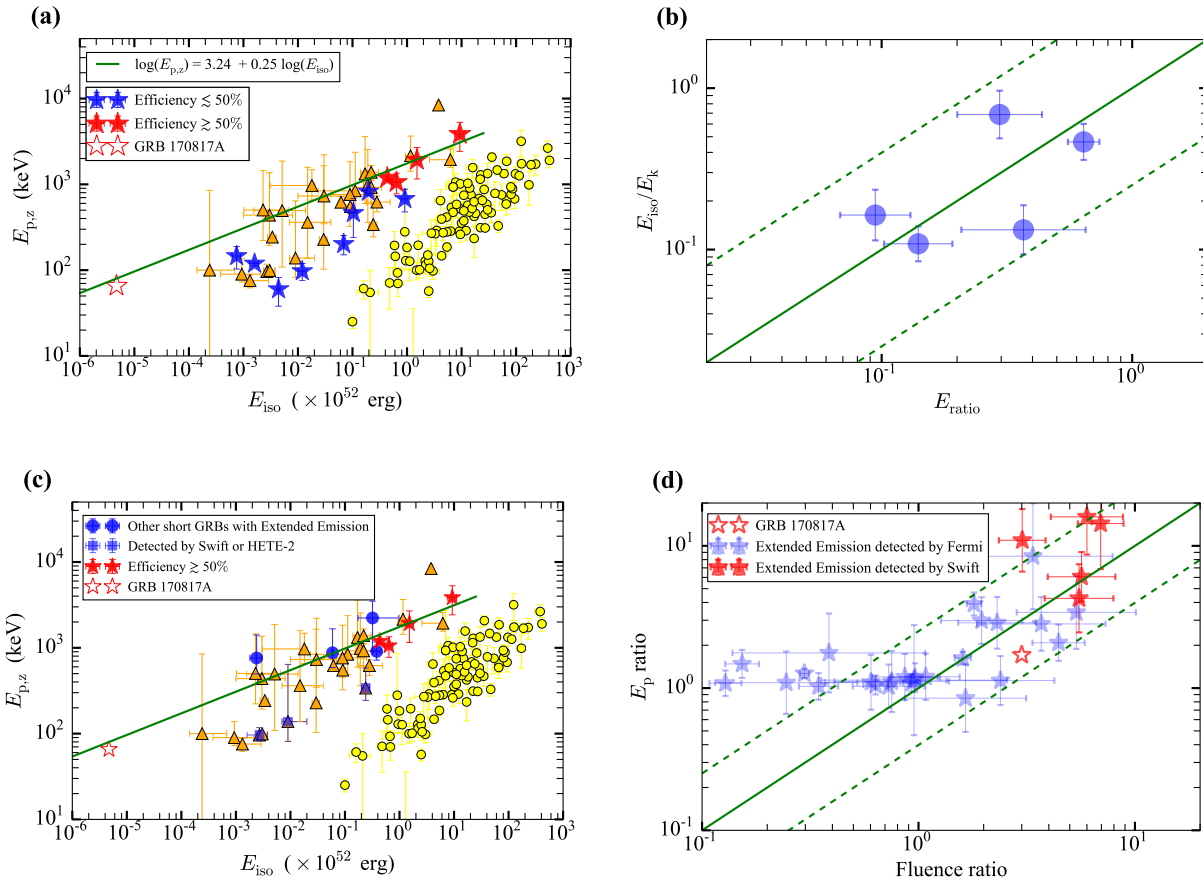


FIG. 5.— Evidence from the short GRBs (see Table 8). (a) The different distributions of E_p and E_{iso} for the two distinguished samples: $\epsilon_\gamma \gtrsim 50\%$ (red stars) and $\epsilon_\gamma \lesssim 50\%$ (blue stars). (b) The distribution of E_{ratio} and E_{iso}/E_k for the $\epsilon_\gamma \lesssim 50\%$ sample (reduced $\chi^2 = 0.140$). (c) The E_p and E_{iso} distribution of the main pulse for other 7 bursts (blue circles and boxes), which have extended emission (see Minaev & Pozanenko 2020) and lack efficiency. Note that all the 5 bursts of the $\epsilon_\gamma \gtrsim 50\%$ sample (red stars) have extended emission, including GRB 170817A. (d) The comparison of the ratios of the E_p and the fluence (or E_{iso}) for the main pulse and the extended emission of a large extended emission sample (reduced $\chi^2 = 0.196$), including the bursts without redshift (blue stars).

are taken, just as $\Delta(L_{X,11h})$ given in D’Avanzo et al. (2012).

3. EVIDENCE FROM LONG GRBS WITH EXTREMELY HIGH EFFICIENCY ($\epsilon_\gamma \gtrsim 80\%$)

There is much controversy about the spectral differences between the photosphere emission model and the synchrotron emission model, after considering the more natural and complicated physical conditions (jet structure, decaying magnetic field, and so on; Uhm & Zhang 2014; Geng et al. 2018; Meng et al. 2018, 2019, 2022). Nevertheless, a crucial difference between these two models is that the photosphere emission model predicts much higher radiation efficiency ϵ_γ . The synchrotron emission models mainly include the internal shock model (for a matter-dominated fireball; Rees & Meszaros 1994) and the ICMART model (internal-collision-induced magnetic reconnection and turbulence, for a Poynting flux-dominated outflow; Zhang & Yan 2011). For the internal shock model, since only the relative kinetic energy between different shells can be released, the radiation efficiency is rather low ($\sim 10\%$; Kobayashi et al. 1997). For the ICMART model, the radiation efficiency can be much higher ($\sim 50\%$), and it reaches $\sim 80\%$ in the extreme case. However, the extremely high ϵ_γ ($\epsilon_\gamma \gtrsim 80\%$)

is unlikely to be achieved, because the magnetic reconnection requires some conditions to be triggered, so much magnetic energy is left. For the photosphere emission model, if only the acceleration is in the unsaturated regime ($R_{\text{ph}} < R_s$), the radiation efficiency can be close to 100%. Thus, in this work, we select the GRBs with extremely high ϵ_γ ($\epsilon_\gamma \gtrsim 80\%$; see Figure 3(a) and Table 1). Note that the two bursts (GRB 990705 and GRB 000210) that are claimed to have extremely high ϵ_γ in Lloyd-Ronning & Zhang (2004) are also included. We then analyze the prompt² and afterglow³ properties of these 15 long GRBs, to confirm the photosphere emission origin.

3.1. Characteristics of Prompt Emission

In Figure 3(b), we plot the E_p and E_{iso} distributions of the selected GRBs (omitting GRB 081203A and GRB 130606A, because of the large E_p error), and we find

² The *Fermi*/GBM data are publicly available at <https://heasarc.gsfc.nasa.gov/W3Browse/fermi/fermigbrst.html>. The Konus-Wind data are publicly available at <https://vizier.cds.unistra.fr/viz-bin/VizieR?source=J/ApJ/850/161>.

³ The X-ray afterglow data are publicly available at https://www.swift.ac.uk/xrt_products/. The optical afterglow data are taken from Li et al. (2012, 2018); Liang et al. (2013).

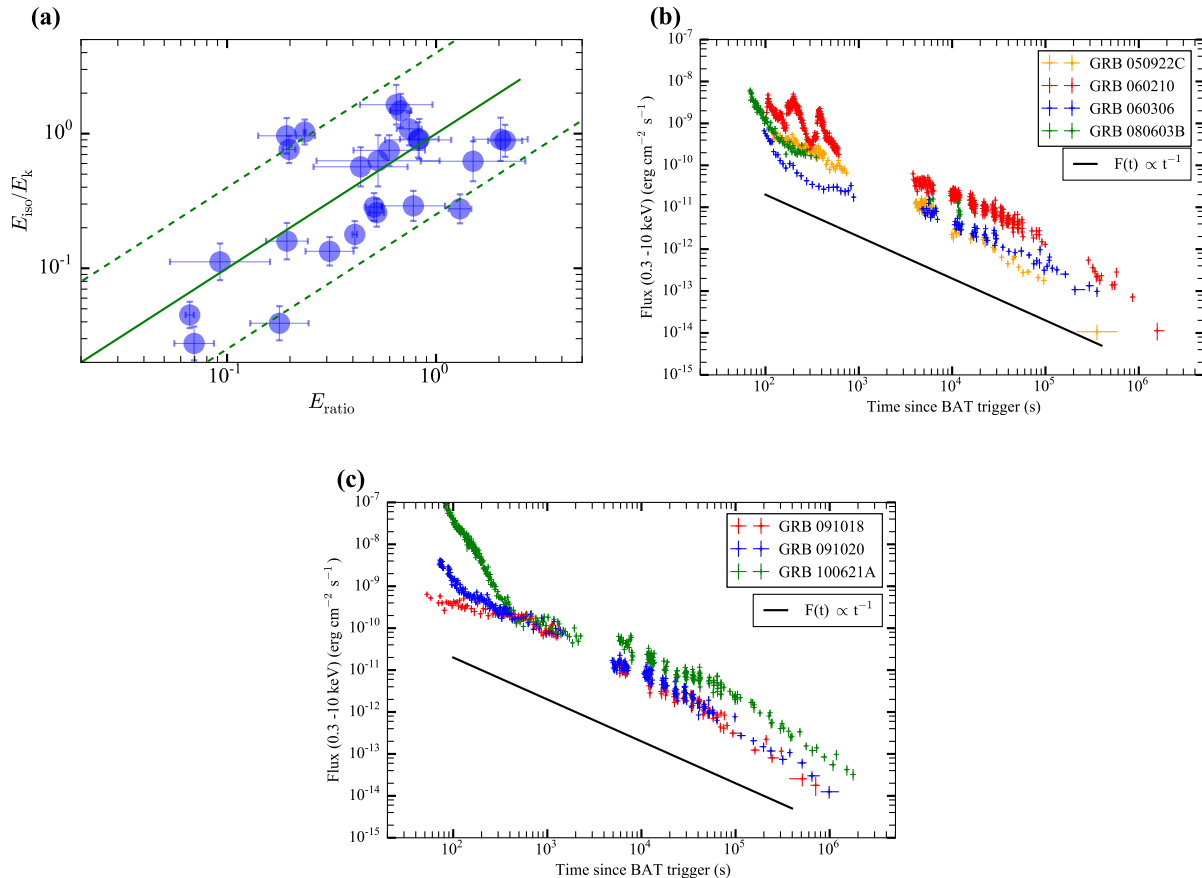


FIG. 6.— The similar observed efficiency (with E_{iso}/E_k from the X-ray afterglow) and theoretically predicted efficiency (from the prompt emission) for the bursts before GRB 110213A (with $L_{X,11h}$ given in D’Avanzo et al. 2012). (a) The distribution of E_{ratio} and E_{iso}/E_k for the $\epsilon_\gamma \lesssim 50\%$ sample, which is found to be well centered around the equal-value line and have a linear correlation (reduced $\chi^2 = 0.160$). (b), (c) The X-ray afterglow light curves for the bursts (7 bursts) with almost same E_{ratio} and E_{iso}/E_k (see Table 5). We find that all these light curves do have a power-law shape with a slope of ~ -1 .

that they follow the predicted $E_p \propto (E_{\text{iso}})^{1/4}$ relation (see Section 2.2.2) quite well. The best-fit result is $\log(E_p) = 2.54 + 0.25 \log(E_{\text{iso}})$. In Figure 3(c), we compare the E_p and E_{iso} distributions of the selected GRBs with those of the large sample of long GRBs, and find that the dispersion is quite small relative to that of the large sample.

In Figure 3(d), we plot the E_p and L_{iso} distributions of the selected GRBs, and find that they also follow the $E_p \propto (L_{\text{iso}})^{1/4}$ relation well. The best-fit result is $\log(E_p) = 2.75 + 0.23 \log(L_{\text{iso}})$. And the dispersion is found to be similar to that of $E_p \propto (E_{\text{iso}})^{1/4}$. Furthermore, based on the best-fit $E_p \sim 10^{2.75} \cdot (L_{\text{iso}})^{1/4}$ and $E_p = 2.7kT_0 = 2.7k(L_{\text{iso}}/4\pi r_0^2 ac)^{1/4}$, we obtain the initial acceleration radius $r_0 \sim 3.21 \times 10^8$ cm, well consistent with the quite high mean value $\langle r_0 \rangle \sim 10^{8.5}$ cm deduced in Pe’er et al. (2015).

In Figure 12, we show the E_p evolutions of the time-resolved spectra for 5 GRBs detected by Fermi/GBM. The E_p evolutions are found to follow the evolution of the flux F quite well (intensity tracking pattern; Liang & Kargatis 1996). This positive correlation is consistent with the abovementioned unsaturated acceleration condition of the photosphere emission. From Tables 1 and 4, we can see that the best-fit spectral model of the

time-integrated spectra is the CPL model, or that the high-energy spectral index β (using the BAND function to fit) is minimal. Thus, the photosphere emission model can better explain the high-energy spectra of these high-efficiency GRBs.

3.2. Characteristics of Afterglows

Figure 13 shows the X-ray afterglow light curves of the selected GRBs (except for GRB 990705 and GRB 000210). We find that all the X-ray afterglow light curves appear as simple power-law shapes⁴, without any plateau, steep decay (Zhang et al. 2006), or significant flare (with weak flares in the early times). In Figure 14, we show the optical afterglow light curves of 6 GRBs whose early peaks can be detected. All the optical afterglow light curves show significant reverse shock signals. The power-law shape of the X-ray afterglow and the reverse shock in the optical afterglow are the basic predictions (Paczynski & Rhoads 1993; Mészáros & Rees 1997; Sari & Piran 1999) of the classical hot fireball model of GRBs (see Appendices B.2 and B.3). Thus, the jets of these high-efficiency GRBs are likely to be thermal-dominated, and the radiation mechanism of the prompt

⁴ Interestingly, a similar X-ray afterglow characteristic has been found for GeV-/TeV-detected GRBs (Yamazaki et al. 2020).

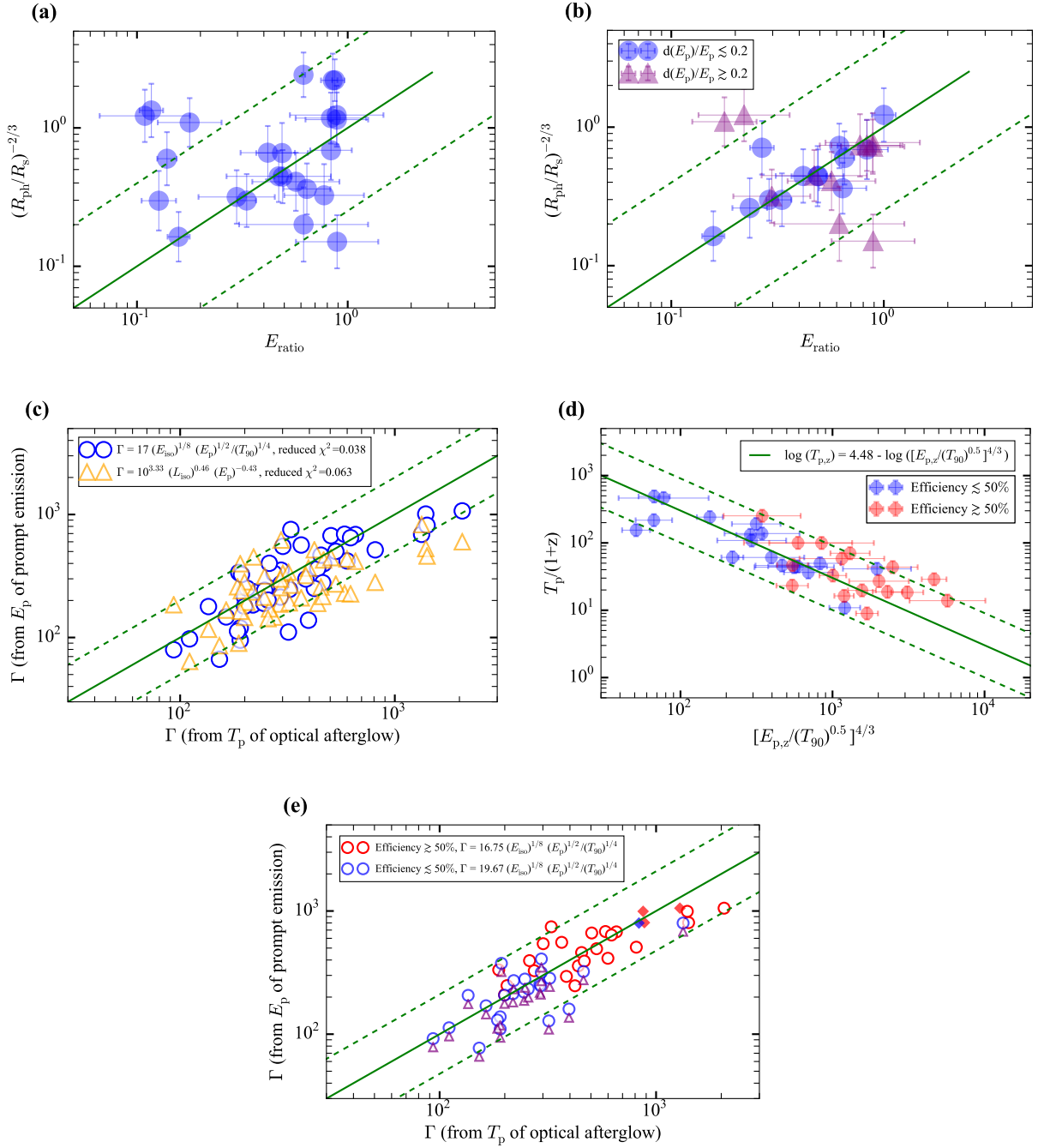


FIG. 7.— The tight correlation of $\Gamma \propto E_{\text{iso}}^{1/8} E_p^{1/2} / (T_{90})^{1/4}$ to estimate Γ , we derived based on the same efficiency of E_{ratio} and $(R_{\text{ph}}/R_s)^{-2/3}$ in the $\epsilon_\gamma \lesssim 50\%$ case (see Table 6). (a) The distribution of E_{ratio} and $(R_{\text{ph}}/R_s)^{-2/3}$ for the selected $\epsilon_\gamma \lesssim 50\%$ sample (based on $E_{\text{ratio}} \leq 0.9$; 24 bursts; reduced $\chi^2 = 0.239$). (b) The distributions of E_{ratio} and $(R_{\text{ph}}/R_s)^{-2/3}$ for the two sub-samples with smaller E_p errors ($dE_p/E_p \leq 0.2$; blue circles; reduced $\chi^2 = 0.025$) and larger E_p errors ($dE_p/E_p \geq 0.2$; purple triangles; reduced $\chi^2 = 0.228$). (c) A comparison of the Γ obtained from the optical afterglow (for 47 bursts in Ghirlanda et al. 2018) and the Γ obtained from the prompt emission (orange triangles for $\Gamma = 10^{3.33} L_{\text{iso}}^{0.46} E_p^{-0.43}$ and blue circles for $\Gamma = 17 \cdot E_{\text{iso}}^{1/8} E_p^{1/2} / (T_{90})^{1/4}$). (d) The distribution of $[E_p/(T_{90})^{1/2}]^{4/3}$ and $T_p/(1+z)$ for 35 bursts (reduced $\chi^2 = 0.100$). (e) The slightly different constants for the $\epsilon_\gamma \lesssim 50\%$ case (Const=19.67, reduced $\chi^2 = 0.034$; Const=16.75, purple triangles, reduced $\chi^2 = 0.048$) and the $\epsilon_\gamma \gtrsim 50\%$ case (Const = 16.75).

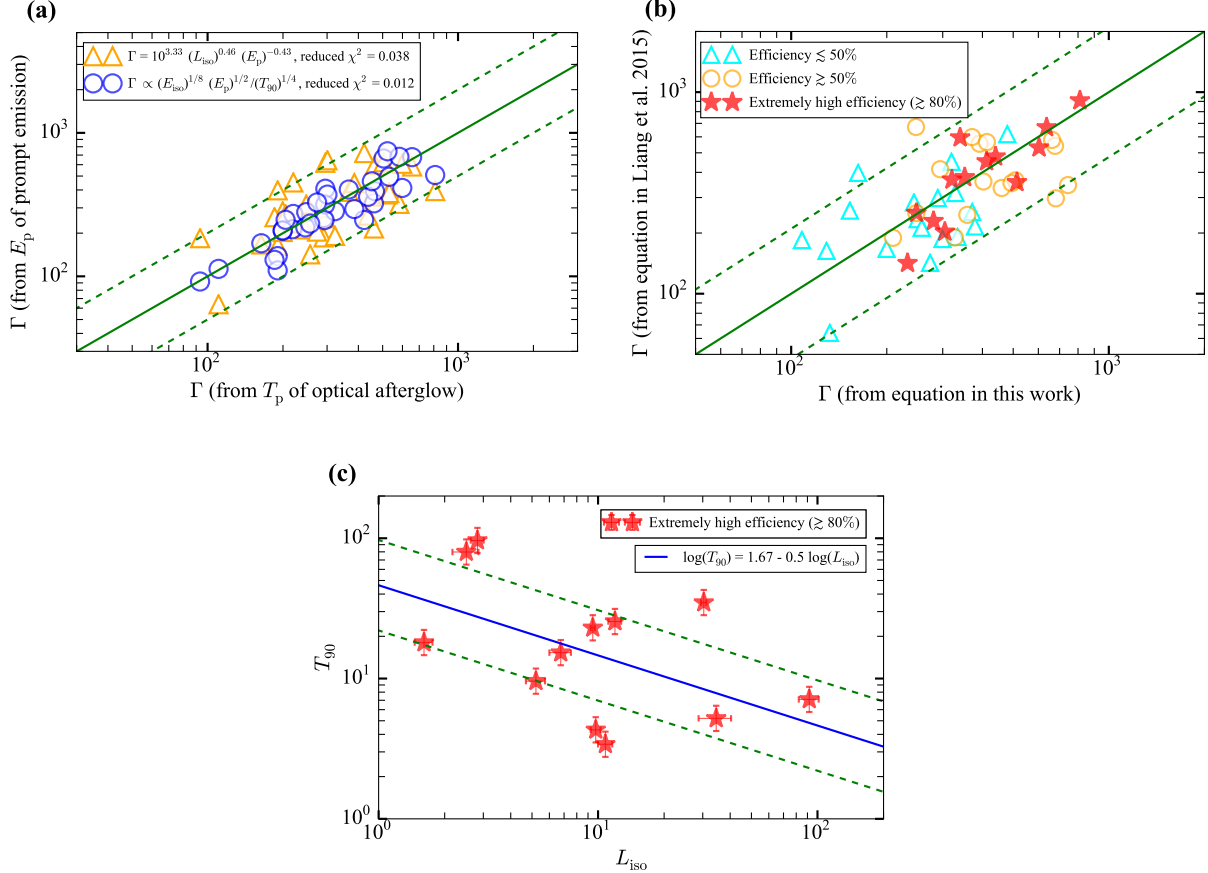


FIG. 8.— Comparison of the Γ obtained from $\Gamma \propto E_{\text{iso}}^{1/8} E_p^{1/2} / (T_{90})^{1/4}$ and $\Gamma = 10^{3.33} L_{\text{iso}}^{0.46} E_p^{-0.43}$ (see Tables 6 and 1). (a) The comparison of the Γ obtained from the optical afterglow and the Γ obtained from the prompt emission (orange triangles for $\Gamma = 10^{3.33} L_{\text{iso}}^{0.46} E_p^{-0.43}$ and blue circles for $\Gamma \propto E_{\text{iso}}^{1/8} E_p^{1/2} / (T_{90})^{1/4}$) for the better sample (35 bursts) in Figure 7(d). The different constants are used for the $\epsilon_\gamma \gtrsim 50\%$ and $\epsilon_\gamma \lesssim 50\%$ sub-samples. (b) Comparison of the Γ obtained from $\Gamma = 10^{3.33} L_{\text{iso}}^{0.46} E_p^{-0.43}$ and $\Gamma \propto E_{\text{iso}}^{1/8} E_p^{1/2} / (T_{90})^{1/4}$ for the $\epsilon_\gamma \lesssim 50\%$ (cyan triangles; reduced $\chi^2 = 0.043$), the $\epsilon_\gamma \gtrsim 50\%$ (orange circles; reduced $\chi^2 = 0.046$) and the high-efficiency ($\epsilon_\gamma \gtrsim 80\%$; red stars; reduced $\chi^2 = 0.017$) sub-samples. Obviously, these two estimations are consistent with each other, since they can be transferred with $E_p \propto (E_{\text{iso}})^{1/4}$. (c) The $T_{90} \propto (L_{\text{iso}})^{-0.5}$ correlation (reduced $\chi^2 = 0.174$), found for the high-efficiency sub-sample ($\epsilon_\gamma \gtrsim 80\%$).

emission is unlikely to be the ICMART model (for Poynting flux-dominated outflow; Zhang & Yan 2011). Also, considering the high efficiency ($\epsilon_\gamma \gtrsim 80\%$), the internal shock model ($\epsilon_\gamma \sim 10\%$; Rees & Meszaros 1994; Kobayashi et al. 1997) is unlikely. The prompt emission of these GRBs is likely to be produced by the photosphere emission, then.

In Figure 1(a), we show the correlation of L_{iso} and Γ for the selected GRBs. The Γ is obtained by the tight $L_{\text{iso}} - E_p - \Gamma$ correlation (Liang et al. 2015; the values are taken from Xue et al. 2019). In Section 4.3, we find that this estimation is likely to be quite accurate for these high-efficiency GRBs with $E_p \propto (L_{\text{iso}})^{1/4}$. Though 4 GRBs have detections of the peak time of the optical afterglow, we do not use them to estimate the Γ , because of the significant reverse shock signals. We find that Γ is tightly correlated with L_{iso} , $\Gamma \propto (L_{\text{iso}})^{0.29}$. This is well consistent with the prediction of the neutrino annihilation from the hyperaccretion disk (Lü et al. 2012), $\Gamma \propto (L_{\text{iso}})^{7/27} = (L_{\text{iso}})^{0.26}$. This therefore also supports the jets of these GRBs being thermal-dominated.

In Figure 1(b), we show the correlation of E_{iso}/E_k and

η/Γ (see Section 2.2.1) for the selected GRBs. According to Equation (10), along with $r_0 \sim 3.21 \times 10^8$ cm, as derived above, and L_{iso} , we can use Γ to obtain the η for each burst. We find the obvious linear correlations for E_{iso}/E_k and η/Γ , and they are almost the same (aside from 3 bursts: note that we obtain 4 bursts that are almost the same when we take $r_0 = 3.21 \times 10^8$ cm, and then use the offset from the best-fit $E_p \propto (L_{\text{iso}})^{1/4}$ relation to slightly modify r_0 for the other bursts, to obtain 3 other bursts that are almost the same) when we take $E_{k,52} = 5 * L_{X,45}$ ($E_{k,52} = E_k/10^{52}$, $L_{X,45} = L_X/10^{45}$; this is quite close to the derivation of $E_{k,52} = 3.7 * L_{X,45}$ described in Section 4.1, and the slight difference is likely to result from the slight error of Γ estimated by the $L_{\text{iso}} - E_p - \Gamma$ correlation). Again, this result strongly supports the photosphere emission origin in the unsaturated acceleration regime for these high-efficiency GRBs.

3.3. Discussion of the Probability Photosphere Model and the Dissipative Photosphere Model

According to the above statements, the prompt emission of the selected high-efficiency GRBs is likely to be

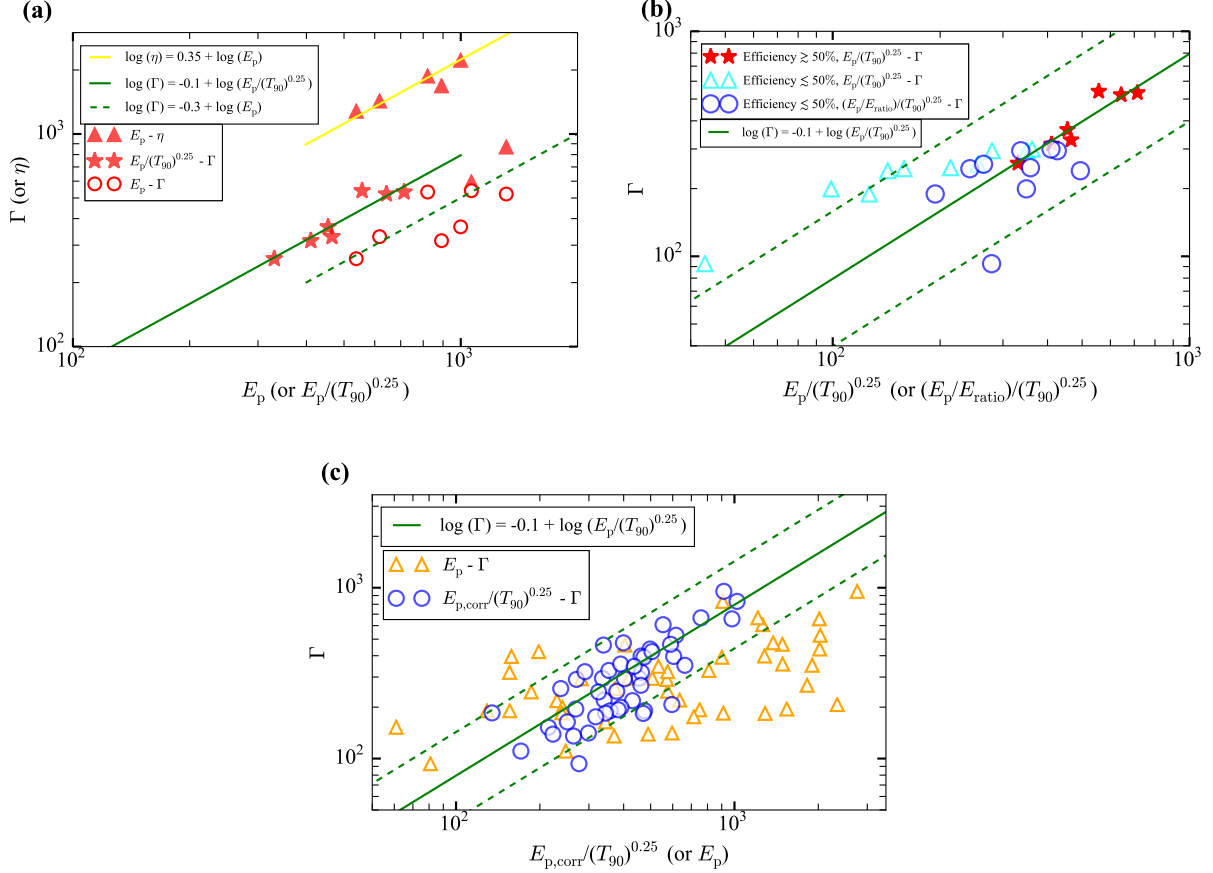


FIG. 9.— The tight correlation of $\Gamma \propto E_p/(T_{90})^{1/4}$, predicted by $\Gamma \propto E_{\text{iso}}^{1/8} E_p^{1/2}/(T_{90})^{1/4}$ and $E_p \propto (E_{\text{iso}})^{1/4}$. (a) The distributions of $E_p - \Gamma$ (red circles; reduced $\chi^2 = 0.013$), $E_p - \eta$ (red triangles; reduced $\chi^2 = 0.002$) and $E_p/(T_{90})^{1/4} - \Gamma$ (red stars; reduced $\chi^2 = 0.002$) for the selected $\epsilon_\gamma \gtrsim 50\%$ sample with T_p detection (7 bursts in Figure 2(e); see Table 3). It is obvious that, the tight correlations of $\Gamma = 10^{-0.1} \cdot E_p/(T_{90})^{1/4}$ and $E_p \propto \eta$ (for the 5 bursts with higher efficiency, thus $\eta \propto (E_{\text{iso}})^{1/4}$) are found. (b) The distributions of $(E_p/E_{\text{ratio}})/(T_{90})^{1/4} - \Gamma$ (blue circles; reduced $\chi^2 = 0.031$) and $E_p/(T_{90})^{1/4} - \Gamma$ (cyan triangles) for the selected $\epsilon_\gamma \lesssim 50\%$ sample with T_p detection (6 bursts in Figure 2(d); see Table 2). The tight correlation of $(E_p/E_{\text{ratio}})/(T_{90})^{1/4} \propto \Gamma$ is found, which is in line with the $E_p/(T_{90})^{1/4} \propto \Gamma$ correlation for the $\epsilon_\gamma \gtrsim 50\%$ case. (c) The distribution of $\Gamma - E_p/(T_{90})^{1/4}$ (blue circles; reduced $\chi^2 = 0.025$) for the large sample with Γ (47 bursts; see Table 6) in Ghirlanda et al. (2018). For the $\epsilon_\gamma \gtrsim 50\%$ case the E_p is re-derived from the $\log(E_p) = 2.54 + 0.25 \log(E_{\text{iso}})$ correlation (using the E_{iso}), and for the $\epsilon_\gamma \lesssim 50\%$ case the E_p is re-derived from E_p/E_{ratio} . Obviously, we find the distribution of Γ and $E_p/(T_{90})^{1/4}$ is well centered around $\Gamma = 10^{-0.1} \cdot E_p/(T_{90})^{1/4}$ and have a linear correlation.

produced by the photosphere emission in the unsaturated acceleration regime. But noteworthy, from Table 1, we can see that the low-energy spectral index α is quite typical (around -1), rather than very hard. This strongly supports that the photosphere emission model having the capacity to produce the observed typical soft low-energy spectrum. Theoretically, the probability photosphere model (with geometric broadening) and the dissipative photosphere model (with subphotospheric energy dissipation) can both achieve this. But for the dissipative photosphere model, the $E_p \propto (E_{\text{iso}})^{1/4}$ relation should be violated, since the inverse Compton scattering below the photosphere radius will change the photon energy (namely $T_{\text{ob}} \neq T_0$; see Appendix A). Also, the high-energy spectrum for this model should be a power law, rather than the exponential cutoff. So the characteristics of the selected high-efficiency GRBs favor the probability photosphere model.

4. EVIDENCE FROM LONG GRBS WITH $\epsilon_\gamma \gtrsim 50\%$ AND $\epsilon_\gamma \lesssim 50\%$

4.1. $\epsilon_\gamma = 50\%$ and Maximum Γ

For the $\epsilon_\gamma = 50\%$ ($R_{\text{ph}} = R_s$) case, with a fixed L_{iso} the observed Lorentz factor Γ in the afterglow phase should be the maximum, because of the following reason. To obtain $\epsilon_\gamma < 50\%$ ($R_{\text{ph}} > R_s$, $R_{\text{ph}} \propto L_{\text{iso}}/\Gamma^3$ and $R_s = \Gamma \cdot r_0$), Γ ($\Gamma = \eta$) should be smaller. Conversely, for $\epsilon_\gamma > 50\%$, η should be larger. And in this case, from Equation (10), we have $\Gamma \propto (L_{\text{iso}}/\eta)^{1/3}$, thus Γ should also be smaller. Note that this maximum Γ exists for the hot fireball, while the corresponding $\epsilon_\gamma = 50\%$ is the prediction of the photosphere emission origin for the prompt emission. The maximum Γ is given as (see also Equation 16 in Ghirlanda et al. 2018)

$$\Gamma_{\text{max}} = \left[\frac{L_{\text{iso}} \sigma_T}{8\pi m_p c^3 r_0} \right]^{1/4}. \quad (15)$$

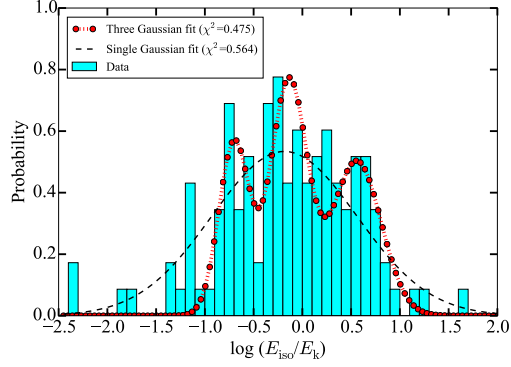


FIG. 10.— The distribution of the E_{iso}/E_k for our whole sample (117 bursts, after GRB 110213A; see Tables 1-3). The mean value is around $\sim 10^{-0.2}$ to $10^{-0.3}$, thus indicating the average efficiency of $\epsilon_\gamma \sim 33\%$ to 40% . Also, the distribution seems to consist of three Gaussian distributions (smaller χ^2 for $E_{\text{iso}}/E_k \gtrsim 10^{-1.0}$).

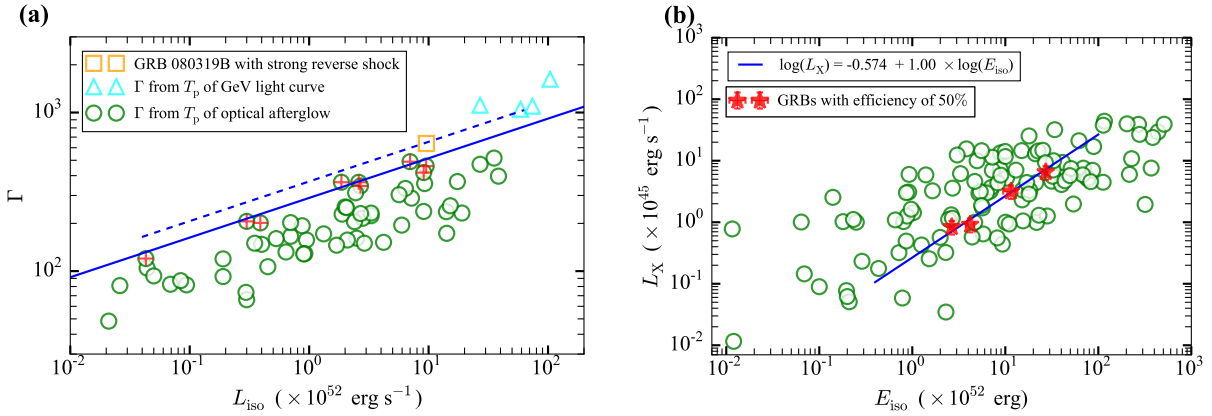


FIG. 11.— The $L_{\text{iso}} - \Gamma$ and $E_{\text{iso}} - L_{X,45}$ distributions for the $\epsilon_\gamma = 50\%$ sample (see Table 7). (a) The distribution of L_{iso} and Γ for the complete sample (62 bursts) with the detection of T_p . We select the sample (9 bursts, marked by the red plus) with the maximum Γ (for fixed L_{iso}), to check whether their efficiency is 50% as predicted by the photosphere emission model. (b) The distribution of E_{iso} and $L_{X,45}$ for the selected sample with the maximum Γ (4 bursts with $L_{X,45}$ detection, red stars). It is found that all these bursts have almost the same efficiency (with $E_{\text{iso}} \propto L_X \propto E_k$, reduced $\chi^2 = 0.008$). Thus, we think that the efficiency ϵ_γ for these bursts is likely to be 50% ($E_{\text{iso},52} = E_{k,52} \simeq 3.7 * L_{X,45}$).

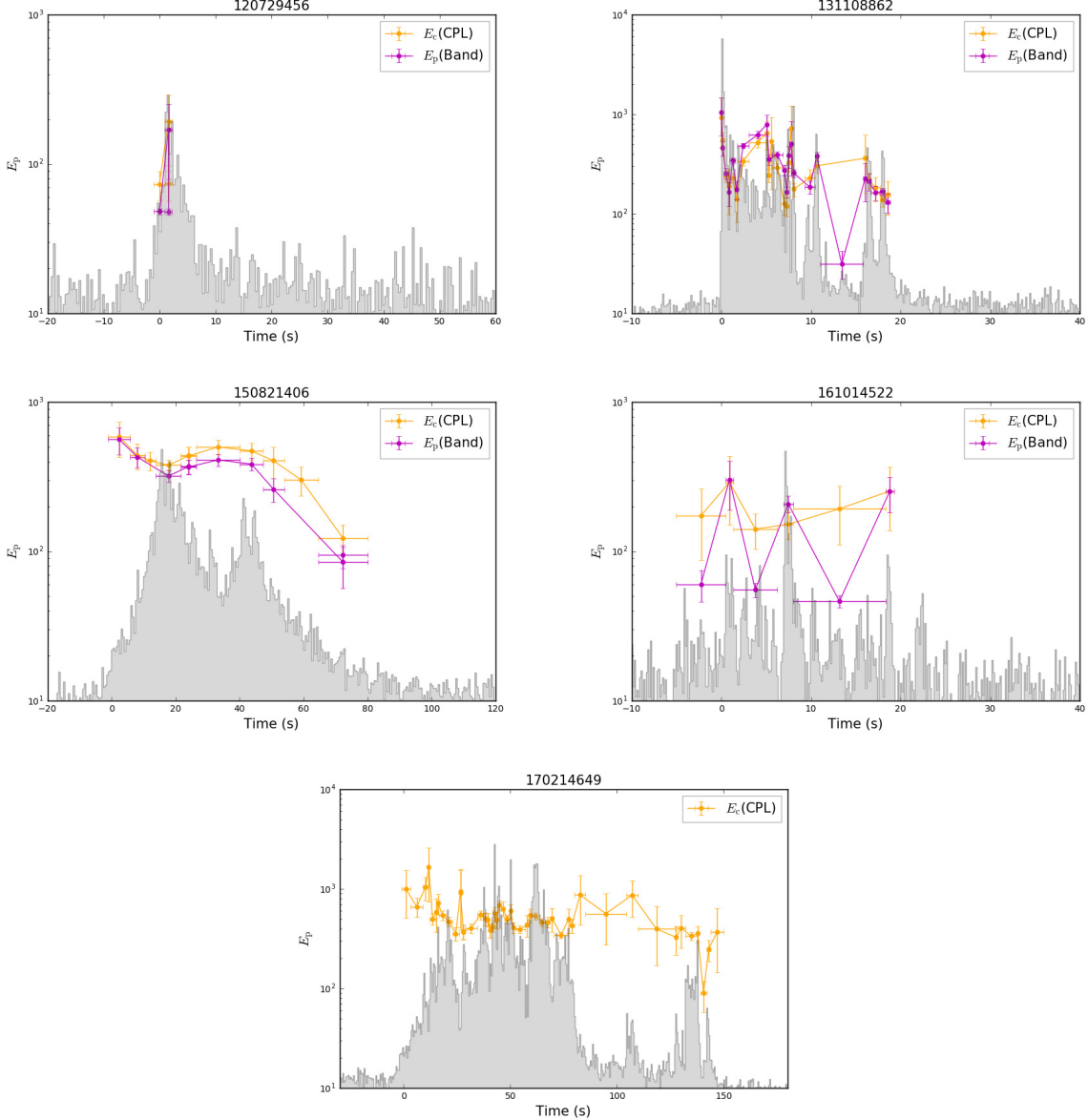


FIG. 12.— The E_p evolutions of the time-resolved spectra for 5 extremely high-efficiency GRBs ($\epsilon_\gamma \gtrsim 80\%$) detected by *Fermi*/GBM. The E_p evolutions almost follow the evolution of the flux F , consistent with the predicted $E_p \propto F^{1/4}$ by the photosphere (thermal) emission in the unsaturated acceleration regime.

In Figure 11(a), we show the distribution of L_{iso} and Γ for the complete sample (62 bursts), with the detection of the peak time of the early optical afterglow (Ghirlanda et al. 2018; obtaining Γ). Obviously, with the exception of GRB 080319B (with a strong reverse shock signal) and 4 bursts (peak time is obtained from the *Fermi*/LAT light curve, and the decay slope of ~ 1.5 implies that it is likely to be produced by the radiative fireball and the Γ should be smaller by a factor of ~ 1.6 , see Ghisellini et al. (2010) and Appendix B.4), the distribution of the maximum Γ well follows the predicted $L_{\text{iso}}^{1/4}$ correlation, and only has the difference of a constant $\sim 10^{0.1}$ (1.27) from the prediction of Equation (15) (the dashed line, $r_0 \sim 3.21 \times 10^8$ cm is used based on Figure 3). Note that though the equation for calculating Γ is confirmed to act as $\Gamma \propto (E_k)^{1/8} \cdot [T_p/(1+z)]^{-3/8}$, its constant is

highly uncertain (see Table 2 in Ghirlanda et al. (2018)). The constant that is given in other works (with different methods) can be 1.7 (or 0.5) times that used in Ghirlanda et al. (2018). So the above difference (1.27) obtained by our work is reasonable, and may be more accurate (since it does not strongly depend on the model assumption; if r_0 is accurate, then it is likely to be accurate).

Then, we select the sample (9 bursts) with the maximum Γ (see Table 7) to check their efficiency properties. In Figure 11(b), we show the distribution of E_{iso} and $L_{X,45}$ for this sample (4 bursts with $L_{X,45}$ detection). Note that we exclude GRB 081007 due to the too small E_{iso} and GRB 080310 due to the plateau in the early optical afterglow. As expected from the photosphere emission model, all these bursts have almost the same efficiency (with $E_{\text{iso}} \propto L_X \propto E_k$). Thus, we think that the efficiency ϵ_γ for these bursts is likely to be 50%

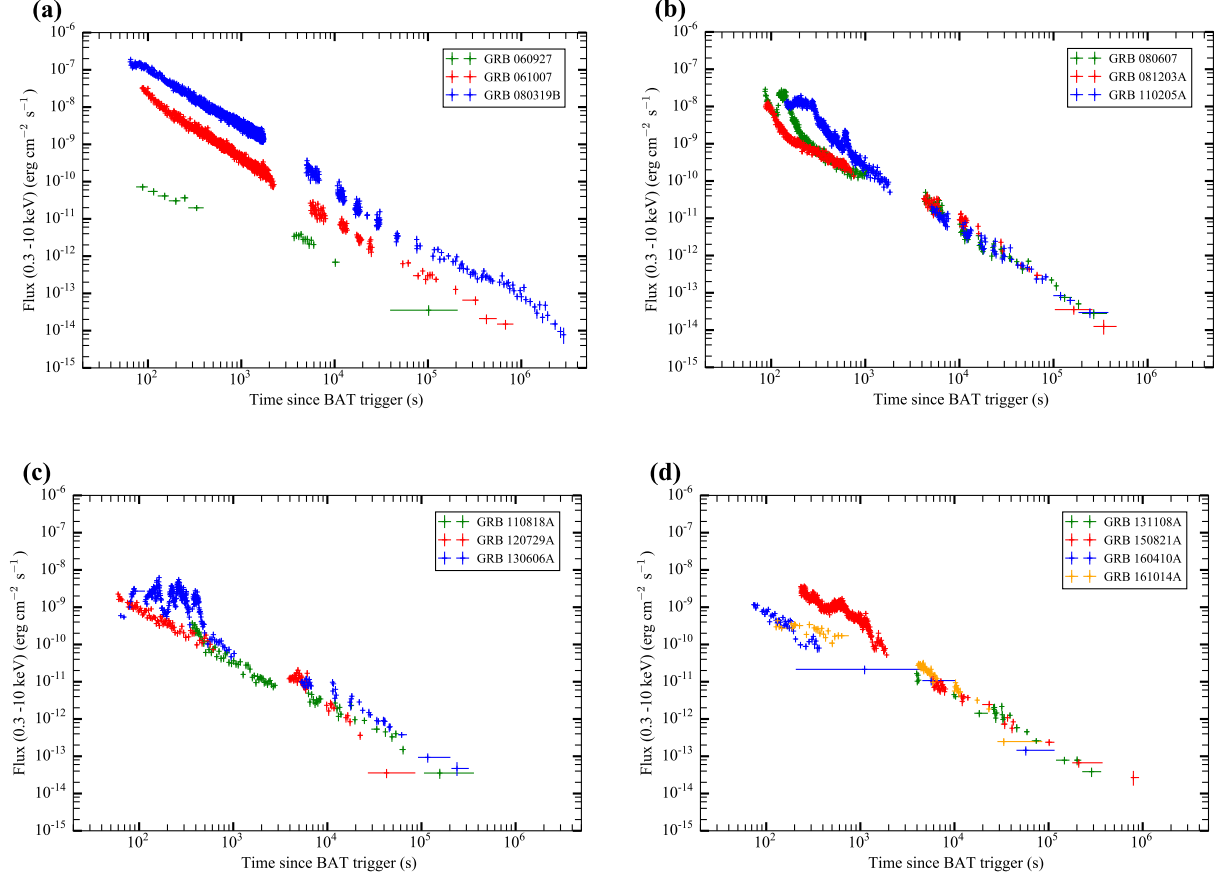


FIG. 13.— The X-ray afterglow light curves for the selected extremely high-efficiency GRBs (except for GRB 990705 and GRB 000210). All these light curves appear as a simple power-law shape, without any plateau, steep decay, or significant flare (with weak flare in the early times).

($E_{\text{iso},52} = E_{k,52} \simeq 3.7 * L_{X,45}$). Note that, based on this, the average derived efficiency ($\epsilon_\gamma \sim 33\%$ to 40% ; see Figure 10) for the whole sample (117 bursts) is almost consistent with that given in other works (Lloyd-Ronning & Zhang 2004; Fan & Piran 2006; Zhang et al. 2007; D’Avanzo et al. 2012; Wygoda et al. 2016).

4.2. $E_p - E_{\text{iso}}$ Distributions and Consistent Efficiency

Based on the derivation of $E_{k,52} = 3.7 * L_{X,45}$ described above, and separated by $E_{\text{iso},52} = E_{k,52} = 3.7 * L_{X,45}$ ($\epsilon_\gamma = 50\%$) for the distribution of $E_{\text{iso},52}$ and $L_{X,45}$ in Figure 11, we obtain two distinguished long-GRB samples ($\epsilon_\gamma \lesssim 50\%$, see Table 2; and $\epsilon_\gamma \gtrsim 50\%$, see Table 3). Note that we exclude the above high-efficiency sample ($\epsilon_\gamma \gtrsim 80\%$) and the sample with $\epsilon_\gamma = 50\%$.

In Figure 4(a), we show that the best-fit result for the $\epsilon_\gamma \gtrsim 50\%$ sample is $\log(E_p) = 2.47 + 0.25 \log(E_{\text{iso}})$, which is consistent with the prediction of the photosphere emission model. Also, this result is almost the same as that for the above high-efficiency sample. The offset from the best-fit result is likely to be caused by a distribution of r_0 (as for the constrained results in Pe’er et al. 2015). For the $\epsilon_\gamma \lesssim 50\%$ sample, E_{iso} and E_p should both decrease by the same factor of $(R_{\text{ph}}/R_s)^{-2/3}$ (see Section 2.2.3), compared with the distribution of $\log(E_p) = 2.54 + 0.25 \log(E_{\text{iso}})$ for the above high-efficiency sample. In Figure 4(a), we show that the upmost distri-

bution for the $\epsilon_\gamma \lesssim 50\%$ sample is well around $\log(E_p) = 2.54 + 0.25 \log(E_{\text{iso}})$, and that the best-fit result (much smaller) is $\log(E_p) = 2.31 + 0.26 \log(E_{\text{iso}})$. The decreases of E_{iso} and E_p are more obvious when we divide the $\epsilon_\gamma \lesssim 50\%$ sample into two subsamples ($\epsilon_\gamma \lesssim 17\%$ and $\epsilon_\gamma \gtrsim 17\%$).

In Figure 2(a), we show the distributions of E_{ratio} ($E_{\text{ratio}} = [(E_p/2.7k)^4 * (4\pi r_0^2 ac)/E_{\text{iso}}]^{1/3}$) and E_{iso}/E_k (implicitly, $E_{k,52} = 3.7 * L_{X,45}/((1+z)/2)$ is adopted) for the $\epsilon_\gamma \lesssim 50\%$ sample. They are well centered around the equal-value line and have a linear correlation. This is well consistent with the prediction from the photosphere emission model (see Section 2.2.4). The dispersion is likely to be caused by the estimation error for E_k (we have excluded the bursts with large E_p errors of $dE_p/E_p \geq 0.2$), since many X-ray afterglow light curves are quite complex (with plateaus, steep decays, or significant flares). The method of using $L_{X,11h}$ to estimate E_k should only be completely correct for X-ray afterglows with power-law shapes and slopes of -1 . To check the origin of the dispersion, we select the bursts with almost the same E_{ratio} and E_{iso}/E_k (see Table 5). As expected, we find that all these bursts (7 bursts) have a power-law X-ray afterglow light curve with a slope of ~ -1 (shown in Figures 2(b) and (c)).

Also, according to Section 2.2.4, for the $\epsilon_\gamma \lesssim 50\%$ sample, we should have $E_{\text{ratio}} = E_{\text{iso}}/E_k = (R_{\text{ph}}/R_s)^{-2/3}$.

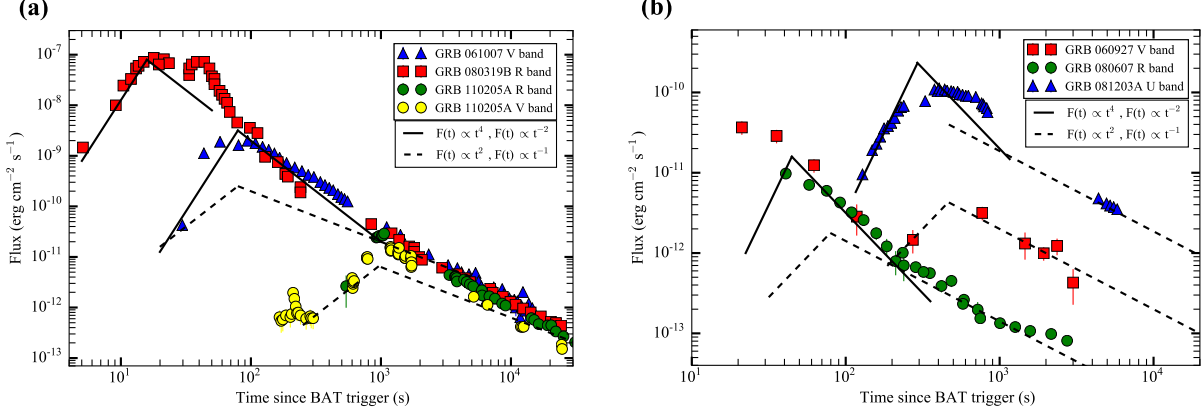


FIG. 14.— The optical afterglow light curves for 6 extremely high-efficiency GRBs ($\epsilon_\gamma \gtrsim 80\%$) whose early peaks can be detected. All these light curves show significant reverse shock signals. (a) 3 GRBs considered also to have reverse shock signals (with detections of both the rapid rise $f \gtrsim t^3$ and fall $f \sim t^{-2}$) in other works (Gao et al. 2015; Yi et al. 2020). (b) 3 GRBs with detection of only the rapid rise $f \gtrsim t^3$ or the rapid fall $f \sim t^{-2}$.

To check this, we select the bursts with detections of the peak time of the optical afterglow (using them to estimate the Γ and thus $(R_{\text{ph}}/R_s)^{-2/3}$). Note that since E_{ratio} and E_{iso}/E_k are the average results for the whole duration, and $(R_{\text{ph}}/R_s)^{-2/3} \propto L^{-2/3}$, we use $L = E_{\text{iso}}/T_{90}$ (rather than L_{iso}). In Figure 2(d), we show the distributions of E_{ratio} , E_{iso}/E_k and $(R_{\text{ph}}/R_s)^{-2/3}$ for the selected sample (6 bursts). Similar to the above, they are well centered around the equal-value line and have a linear correlation. Also, 1 burst has almost the same values for these three quantities, and the other 5 bursts have almost the same values for two quantities. So the predicted $E_{\text{ratio}} = E_{\text{iso}}/E_k = (R_{\text{ph}}/R_s)^{-2/3}$ from the photosphere emission model can be well reproduced.

For the $\epsilon_\gamma \gtrsim 50\%$ sample, similar to Figure 1(b) (for the high-efficiency GRBs), we should have $E_{\text{iso}}/E_k = \eta/\Gamma$. To check this, we also select the bursts with detections of the peak time of the optical afterglow (using them to estimate Γ and thus η). Note that since $\Gamma \propto L^{1/3}$ and the derived Γ is likely to correspond to L_{iso} (the maximum L), we use $L = L_{\text{iso}}$ when calculating η . In Figure 2(e), we show the distribution of E_{iso}/E_k and η/Γ for the selected sample (7 bursts). As expected, they are well centered around the equal-value line and have a linear correlation.

The analysis results obtained above are for the sample with $L_{X,11h}$ as derived in this work (for GRBs after GRB 110213A). For another sample with $L_{X,11h}$ presented in D’Avanzo et al. (2012) (for GRBs before GRB 110213A), we perform a similar analysis and obtain similar results. For the $\epsilon_\gamma \gtrsim 50\%$ sub-sample, the E_p and E_{iso} distribution is also centered around $\log(E_p) = 2.47 + 0.25 \log(E_{\text{iso}})$ (see Figure 4(b)). For the $\epsilon_\gamma \lesssim 50\%$ sub-sample, the decreases of E_{iso} and E_p are also obvious. Also, the distributions of E_{ratio} and E_{iso}/E_k are well centered around the equal-value line, and have linear correlations (see Figure 6(a)). For the selected bursts with almost same E_{ratio} and E_{iso}/E_k (see Table 5), all (7 bursts) show a power-law X-ray afterglow light curve with a slope of ~ -1 (see Figures 6(b) and (c)).

4.3. The Excellent Derived $\Gamma \propto E_{\text{iso}}^{1/8} E_p^{1/2} / (T_{90})^{1/4}$ Correlation

The small burst number in Figure 2(d) is a result of obtaining both the X-ray afterglow light curve and the detection of the peak time of the early optical afterglow. To further check $E_{\text{ratio}} = E_{\text{iso}}/E_k = (R_{\text{ph}}/R_s)^{-2/3}$ for the $\epsilon_\gamma \lesssim 50\%$ case, we then analyze the complete sample with detections of the peak time of the early optical afterglow (obtaining Γ and thus $(R_{\text{ph}}/R_s)^{-2/3}$; Ghirlanda et al. 2018; see Table 6). Note that the used constant is 1.27 times that given in Ghirlanda et al. (2018) (see Section 4.1). Though lacking of E_{iso}/E_k for most bursts in the sample, considering the different distributions of E_p and E_{iso} for $\epsilon_\gamma \lesssim 50\%$ and $\epsilon_\gamma \gtrsim 50\%$, we can use the judgment of ($E_{\text{ratio}} \lesssim 0.9$) to roughly select the $\epsilon_\gamma \lesssim 50\%$ sub-sample. Note that we do not use the bursts without the E_p value in Minaev & Pozanenko (2020) and Xue et al. (2019) due to the large E_p errors, and we move 4 bursts to the $\epsilon_\gamma \gtrsim 50\%$ sub-sample based on their detections of E_{iso}/E_k . In Figure 7(a), we show the distribution of E_{ratio} and $(R_{\text{ph}}/R_s)^{-2/3}$ for the selected $\epsilon_\gamma \lesssim 50\%$ sub-sample (24 bursts). This distribution is roughly centered around the equal-value line, and has a linear correlation. After modifying the Γ or E_p based on Figure 2(d) (using $E_{\text{ratio}} = E_{\text{iso}}/E_k = (R_{\text{ph}}/R_s)^{-2/3}$) for the 6 bursts there, in Figure 7(b), we show the distributions of E_{ratio} and $(R_{\text{ph}}/R_s)^{-2/3}$ for the two sub-samples with smaller E_p errors ($dE_p/E_p \leq 0.2$) and larger E_p errors ($dE_p/E_p \geq 0.2$). Obviously, for the sub-sample with smaller E_p errors, the values of E_{ratio} and $(R_{\text{ph}}/R_s)^{-2/3}$ are almost the same. Note that we decrease the Γ of GRB 090926A by a factor of 1.6, since its peak time is obtained from the LAT light curve and the decay slope of ~ 1.5 implies that it is likely to be produced by the radiative fireball (Ghisellini et al. 2010). And, for the large offset in Figure 7(b) (the upper offset), we check its (GRB 090618) optical afterglow light curve, and find that the reverse shock signal is significant, thus overestimating the Γ and $(R_{\text{ph}}/R_s)^{-2/3}$.

Based on $E_{\text{ratio}} = (R_{\text{ph}}/R_s)^{-2/3}$, we derive $\Gamma \propto E_{\text{iso}}^{1/8} E_p^{1/2} / (T_{90})^{1/4}$ (see Equation (6) and Equation (7)

in Section 2.2.5). In Figure 7(c), we show a comparison of the Γ obtained from the optical afterglow (for 47 bursts in Ghirlanda et al. 2018) and the Γ obtained from the prompt emission (orange triangles for $\Gamma = 10^{3.33} L_{\text{iso}}^{0.46} E_p^{-0.43}$ and blue circles for $\Gamma = 17 \cdot E_{\text{iso}}^{1/8} E_p^{1/2} / (T_{90})^{1/4}$). Obviously, using these two correlations, we can give an approximate estimation for Γ , both. Furthermore, the Equation (7) derived in our work from the photosphere emission model can give a better estimation for Γ (with a smaller reduced χ^2).

According to Equation (7), two correlations of $T_p/(1+z) \propto [E_p/(T_{90})^{1/2}]^{-4/3}$ (see Section 2.2.6) and $\Gamma \propto E_p/(T_{90})^{1/4}$ (see Section 2.2.7) are predicted, which will be tested in the following section.

4.3.1. $T_p/(1+z) \propto [E_p/(T_{90})^{1/2}]^{-4/3}$ test

In Figure 7(d) we show the distribution of $E_p/(T_{90})^{1/2}$ and $T_p/(1+z)$ for 35 bursts (we delete 7 bursts with $dE_p/E_p \geq 0.2$ and 5 bursts with LAT light curves, and we modify the E_p or T_p for 5 bursts based on Figure 2(d)). Just as predicted, this distribution shows a linear correlation with a slope of $\sim -4/3$, and it is consistent with $T_p/(1+z) \propto (E_p)^{-1.25}$ presented in Table 1 of Ghirlanda et al. (2018). So Equation (7) is likely to be correct.

Besides, from Figure 7(d), we can see that the T_p for the sub-sample of $\epsilon_\gamma \gtrsim 50\%$ is a bit larger than that for $\epsilon_\gamma \lesssim 50\%$, though both satisfy the $T_p/(1+z) \propto [E_p/(T_{90})^{1/2}]^{-4/3}$ correlation. This is well consistent with the slightly different predicted constants of Equation (7) for the $\epsilon_\gamma \lesssim 50\%$ case (19.67, see Equation (8)) and the $\epsilon_\gamma \gtrsim 50\%$ case (16.75, see Equation (11)).

The smaller constant (16.75) for the $\epsilon_\gamma \gtrsim 50\%$ case is consistent with the larger T_p in Figure 7(d). In Figure 7(e), we show the derived Γ using the Equation (8) and the Equation (11), and find that the distribution for the $\epsilon_\gamma \lesssim 50\%$ case is better (more symmetric) than that in Figure 7(c).

4.3.2. $\Gamma = 10^{-0.1} \cdot E_p/(T_{90})^{1/4}$ correlation

In Figure 9(a), we do find the tight correlation of

$$\Gamma = 10^{-0.1} \cdot E_p/(T_{90})^{1/4} \quad (16)$$

for the $\epsilon_\gamma \gtrsim 50\%$ case (with $L_{X,11h}$ detection). Note that the E_p here is re-derived from the $\log(E_p) = 2.54 + 0.25 \log(E_{\text{iso}})$ correlation (using the E_{iso}), since the observed E_p with an offset from the above line is likely to arise from the different r_0 (actually $E_p \propto (E_{\text{iso}}/r_0^2)^{1/4}$) or the error of E_p . Besides, we modify the Γ (using E_{iso}/E_k , mainly for 3 bursts) based on Figure 2(e). In Figure 9(a), we also show the distributions for $E_p - \Gamma$ and $E_p - \eta$, here η is obtained by $\eta/\Gamma = E_{\text{iso}}/E_k$. It is obvious that there is a tight correlation of $E_p \propto \eta$ for the sub-sample (5 bursts) with higher efficiency. This means that $\eta \propto (E_{\text{iso}})^{1/4}$, which is well consistent with the prediction of the neutrino annihilation from the hyperaccretion disk (for the hot fireball).

For the $\epsilon_\gamma \lesssim 50\%$ case, since $(E_p/E_{\text{ratio}}) \propto (E_{\text{iso}}/E_{\text{ratio}})^{1/4}$ and $\Gamma \propto (L_{\text{iso}}/E_{\text{ratio}})^{1/4}$ we should have

$\Gamma \propto (E_p/E_{\text{ratio}})/(T_{90})^{1/4}$. From Figure 9(b) we do find this correlation, which is also in line with that for the $\epsilon_\gamma \gtrsim 50\%$ case. Note that we modify the E_p or Γ based on Figure 2(d). In Figure 9(c) we show the distribution of $\Gamma - E_p/(T_{90})^{1/4}$ for the large Γ sample (47 bursts) in Ghirlanda et al. (2018). Note that for the $\epsilon_\gamma \gtrsim 50\%$ case, the E_p is re-derived from the $\log(E_p) = 2.54 + 0.25 \log(E_{\text{iso}})$ correlation (using the E_{iso}), and for the $\epsilon_\gamma \lesssim 50\%$ case, the E_p is re-derived from E_p/E_{ratio} . For the $\epsilon_\gamma \gtrsim 50\%$ case, when calculating Γ , we modify the E_k based on the original η/Γ . Obviously, we find that the distribution of Γ and $E_p/(T_{90})^{1/4}$ is well centered around $\Gamma = 10^{-0.1} \cdot E_p/(T_{90})^{1/4}$ and shows a linear correlation. Note that the $\Gamma - E_p$ correlation is also found in Ghirlanda et al. (2012).

4.3.3. The consistency of our $\Gamma \propto E_{\text{iso}}^{1/8} E_p^{1/2} / (T_{90})^{1/4}$ correlation and the $\Gamma = 10^{3.33} L_{\text{iso}}^{0.46} E_p^{-0.43}$ correlation

For the better sample (35 bursts) in Figure 7(d), in Figure 8(a), we replot the comparison of the Γ obtained from the optical afterglow and the Γ obtained from the prompt emission (orange triangles for $\Gamma = 10^{3.33} L_{\text{iso}}^{0.46} E_p^{-0.43}$ and blue circles for $\Gamma \propto E_{\text{iso}}^{1/8} E_p^{1/2} / (T_{90})^{1/4}$). For the $\epsilon_\gamma \gtrsim 50\%$ sub-sample (17 bursts) and the $\epsilon_\gamma \lesssim 50\%$ sub-sample (18 bursts), we use the different derived constants. Obviously, the Equation (7) derived in our work gives a much better estimation of Γ (with a much smaller reduced χ^2 , compared with Figure 7(c)). Noteworthy, the $\Gamma = 10^{3.33} L_{\text{iso}}^{0.46} E_p^{-0.43}$ correlation obtained from the statistical fitting is actually consistent with our $\Gamma \propto E_{\text{iso}}^{1/8} E_p^{1/2} / (T_{90})^{1/4}$ correlation derived from the photosphere emission model. Because, along with $E_p \propto (E_{\text{iso}})^{1/4}$ (or $E_p \propto (L_{\text{iso}})^{1/4}$; see Figures 3 and 4), they can be transferred to each other, as shown in the following:

$$\begin{aligned} \Gamma &\propto E_{\text{iso}}^{1/8} E_p^{1/2} / (T_{90})^{1/4} \\ &\propto (E_{\text{iso}}/T_{90})^{1/8} \cdot E_p^{1/2} / (T_{90})^{1/8}, \text{ with } E_p \propto (L_{\text{iso}})^{1/4} \\ &\propto (L_{\text{iso}})^{1/8} \cdot (L_{\text{iso}}^{0.23} \cdot E_p^{-0.43}) / (T_{90})^{1/8} \\ &\propto L_{\text{iso}}^{0.36} \cdot E_p^{-0.43} / (T_{90})^{1/8}, \text{ with } T_{90} \propto (L_{\text{iso}})^{-0.5} \\ &\propto L_{\text{iso}}^{0.36} \cdot E_p^{-0.43} / (L_{\text{iso}}^{-0.5})^{1/8} \\ &\propto L_{\text{iso}}^{0.43} \cdot E_p^{-0.43}. \end{aligned} \quad (17)$$

Here, the adopted $T_{90} \propto (L_{\text{iso}})^{-0.5}$ correlation is found from Figure 8(c) for the high-efficiency sub-sample ($\epsilon_\gamma \gtrsim 80\%$).

In Figure 8(b), we compare the Γ obtained from $\Gamma = 10^{3.33} L_{\text{iso}}^{0.46} E_p^{-0.43}$ and the Γ obtained from $\Gamma \propto E_{\text{iso}}^{1/8} E_p^{1/2} / (T_{90})^{1/4}$ for the $\epsilon_\gamma \gtrsim 50\%$ sub-sample (17 bursts), the $\epsilon_\gamma \lesssim 50\%$ sub-sample (18 bursts) and the high-efficiency sub-sample ($\epsilon_\gamma \gtrsim 80\%$). Obviously, these two estimations are well centered around the equal-value line and have linear correlations. Furthermore, for the high-efficiency sub-sample, which has the tightest $E_p \propto (E_{\text{iso}})^{1/4}$ correlation (with very small dispersion; see Figure 3), these two estimations are almost identical. For the $\epsilon_\gamma \gtrsim 50\%$ sub-sample and the $\epsilon_\gamma \lesssim 50\%$ sub-sample,

which have larger dispersions for the $E_p \propto (E_{\text{iso}})^{1/4}$ correlation, the above two estimations show larger dispersion, also.

4.4. The Distribution of the E_{iso}/E_k for the Whole Sample

In Figure 10, we show the distribution of the E_{iso}/E_k (indicating the efficiency ϵ_γ) for the whole sample (117 bursts). The average value is around $\sim 10^{-0.2}$ to $10^{-0.3}$, thus indicating an average efficiency of $\epsilon_\gamma \sim 33\%$ to 40% . From Figure 10, we also find that the distribution seems to consist of three Gaussian distributions. The high-efficiency peak ($\sim 10^{0.6}$) is almost consistent with the $\eta \propto 10^{0.35} \cdot E_p$ and $\Gamma \propto 10^{-0.3} \cdot E_p$ correlations (namely, $E_{\text{iso}}/E_k = \eta/\Gamma \sim 10^{0.65}$) in Figure 9(a). Theoretically, for the $\epsilon_\gamma > 50\%$ case, from Equation (10) and $\eta \propto (L_{\text{iso}})^{1/4}$, we should also have $\Gamma \propto (L_{\text{iso}}/\eta)^{1/3} \propto (L_{\text{iso}}/L_{\text{iso}}^{1/4})^{1/3} \propto (L_{\text{iso}})^{1/4}$. So the high-efficiency peak is predicted to exist. For the $\epsilon_\gamma < 50\%$ case, $E_{\text{iso}}/E_k = (R_{\text{ph}}/R_s)^{-2/3} \propto (L_{\text{iso}}/\Gamma^4)^{-2/3}$. Thus, the low-efficiency peak ($\sim 10^{-0.7}$) is the natural result of $\Gamma \propto (L_{\text{iso}})^{1/4}$, where $\Gamma = \eta$.

5. EVIDENCE FROM SHORT GRBS WITH $\epsilon_\gamma \gtrsim 50\%$ AND $\epsilon_\gamma \lesssim 50\%$.

For the short GRBs, similar to the long GRBs, we use the judgment of $E_{\text{iso},52} = E_{k,52} = 3.7 * L_{X,45}$ ($\epsilon_\gamma = 50\%$) to obtain the $\epsilon_\gamma \gtrsim 50\%$ sample (4 bursts) and the $\epsilon_\gamma \lesssim 50\%$ sample (8 bursts; see Table 8). In Figure 5(a), we show the E_p and E_{iso} distributions for these two distinguished samples. Obviously, the $\epsilon_\gamma \gtrsim 50\%$ sample and the up-most distribution for the large sample of short GRBs (Zhang et al. 2018b) (without $L_{X,45}$ detections for most) do follow the $E_p \propto (E_{\text{iso}})^{1/4}$ correlation, well consistent with the prediction of the photosphere emission model. Noteworthy, the distribution for GRB 170817A well fits the above line ($\log(E_p) = 3.24 + 0.25 \log(E_{\text{iso}})$), too. For the $\epsilon_\gamma \lesssim 50\%$ sample, as predicted, the distribution is below this line (since E_p and E_{iso} are smaller). Similar to Figure 2(a) (to test whether the E_p and E_{iso} are both smaller by a factor of $E_{\text{iso}}/E_k = (R_{\text{ph}}/R_s)^{-2/3}$), in Figure 5(b) we show the distribution of E_{ratio} ($E_{\text{ratio}} = [(E_p/2.7k)^4 * (4\pi r_1^2 ac)/E_{\text{iso}}]^{1/3}$) and E_{iso}/E_k for this $\epsilon_\gamma \lesssim 50\%$ sample. Note that we exclude 3 bursts with $E_{\text{iso}} \leq 10^{50}$ erg and that we have $r_1 = 3.4 \times 10^7$ cm here. Again as predicted, they are found to be almost centered around the equal-value line, and have a linear correlation.

Interestingly, we find that all the bursts of the $\epsilon_\gamma \gtrsim 50\%$ sample (5 bursts, including GRB 170817A) have extended emission, and the E_p and E_{iso} distribution in Figure 5(a) is for their main pulse. To further test this finding, in Figure 5(c) we show the E_p and E_{iso} distribution of the main pulse for 7 other bursts that have extended emission (Minaev & Pozanenko 2020). It is found that, except for 3 bursts only detected by *Swift* or HETE-2 (lacking the detections in the high-energy band), other 4 bursts do follow the $\log(E_p) = 3.24 + 0.25 \log(E_{\text{iso}})$ correlation of the $\epsilon_\gamma \gtrsim 50\%$ sample, supporting the above finding again. The true E_p values for these 3 outliers are likely to be much larger. According to the above, the main pulse for the short GRBs with extended emission is

likely to be produced by the photosphere emission in the unsaturated acceleration regime. Then, considering the smaller values of both the E_p and E_{iso} for their extended emission, we think that the extended emission may be produced by the transition from the unsaturated acceleration to the saturated acceleration (E_p and E_{iso} are both smaller by the same factor of $E_{\text{iso}}/E_k = (R_{\text{ph}}/R_s)^{-2/3}$). To test this hypothesis, in Figure 5(d), we show the comparison of the ratios of the E_p and the fluence of the main pulse and the extended emission for a large extended emission sample (including the *Swift*/BAT bursts with redshift; Gompertz et al. 2020; and the *Fermi*/GBM bursts without redshift; Lan et al. 2020). As predicted, these two ratios are found to be almost centered around the equal-value line and they have linear correlations.

6. SUMMARY

In this work, after obtaining the prompt emission efficiency of a large GRB sample with redshift, we divide that GRB sample into three sub-samples ($\epsilon_\gamma \gtrsim 80\%$, $\epsilon_\gamma \gtrsim 50\%$, and $\epsilon_\gamma \lesssim 50\%$). Then, the well-known Amati relation (Amati et al. 2002) is well explained by the photosphere emission model. Furthermore, for each sub-sample, the X-ray and optical afterglow characteristics are well consistent with the predictions of the photosphere emission model. Ultimately, large amounts of convincing observational evidence for the photosphere emission model are revealed for the first time.

ACKNOWLEDGEMENTS

I thank the anonymous referee for the constructive suggestions. I thank Bin-Bin Zhang and Liang Li for helpful discussions. Y.-Z.M. is supported by the National Postdoctoral Program for Innovative Talents (grant no. BX20200164). This work is supported by the National Key Research and Development Programs of China (2018YFA0404204), the National Natural Science Foundation of China (grant Nos. 11833003, U2038105, 12121003), the science research grants from the China Manned Space Project with No.CMS-CSST-2021-B11, and the Program for Innovative Talents, Entrepreneur in Jiangsu. I also acknowledge the use of public data from the Fermi Science Support Center, the *Swift* and the Konus-Wind.

APPENDIX A: THE PROBABILITY PHOTOSPHERE MODEL AND THE DISSIPATIVE PHOTOSPHERE MODEL

A.1. THE PROBABILITY PHOTOSPHERE MODEL

For the traditional photosphere model, the photosphere emission is all emitted at the photospheric radius R_{ph} , where the optical depth for a photon propagating towards the observer is equal to unity ($\tau = 1$). But, if only there is an electron at any position, the photon should have a probability to be scattered there. For an expanding fireball, the photons can be last scattered at any place in the fireball with a certain probability. Thus, the traditional spherical shell photosphere is changed to a probability photosphere, namely the probability photosphere model (Pe'er 2008). Based on careful theoretical derivation, the probability function $P(r, \Omega)$, denoting the probability for a photon to be last scattered at the radius r and angular coordinate Ω , can be given as (Pe'er 2008;

Beloborodov 2011; Lundman et al. 2013)

$$P(r, \Omega) = (1 + \beta) D^2 \times \frac{R_{\text{ph}}}{r^2} \exp\left(-\frac{R_{\text{ph}}}{r}\right), \quad (18)$$

where β is the jet velocity and $D = [\Gamma(1 - \beta \cdot \cos \theta)]^{-1}$ is the Doppler factor.

For the probability photosphere model, the observed photosphere spectrum is the overlapping of a series of blackbodies with different temperatures, thus its low-energy spectrum is broadened. After considering the jet with angular structure (e.g., Dai & Gou 2001; Rossi et al. 2002; Zhang & Mészáros 2002), the observed typical low-energy photon index $\alpha \sim -1.0$ (Kaneko et al. 2006; Zhang et al. 2011), spectral evolution and E_p evolutions (hard-to-soft evolution or E_p -intensity tracking; Liang & Kargatis 1996; Lu et al. 2010, 2012) can be reproduced (Lundman et al. 2013; Meng et al. 2019, 2022).

A.2. THE DISSIPATIVE PHOTOSPHERE MODEL

The dissipative photosphere model (or the sub-photosphere model) considers that there is an extra energy dissipation process in the area of moderate optical depth ($1 < \tau < 10$; the sub-photosphere). Different dissipative mechanisms have been proposed, such as shocks (Rees & Mészáros 2005), magnetic reconnection (Gianios & Spruit 2007) and proton-neutron nuclear collisions (Vurm & Beloborodov 2016; Beloborodov 2017). Then, relativistic electrons (with a higher temperature than that of the photons) are generated that upscatter the thermal photons to obtain the non-thermal (broadened) high-energy spectrum.

APPENDIX B: SOME THEORETICAL DESCRIPTIONS FOR THE AFTERGLOW

B.1. THE REMAINING KINETIC ENERGY IN THE AFTERGLOW PHASE (E_k) AND THE ISOTROPIC X-RAY AFTERGLOW LUMINOSITY AT 11 HOURS ($L_{X,11\text{h}}$).

In the context of the standard afterglow model (Paczynski & Rhoads 1993; Mészáros & Rees 1997), since at a late afterglow epoch (11 hours) the X-ray band is above the cooling frequency ν_c , the late-time X-ray afterglow luminosity ($L_{X,11\text{h}}$) only sensitively depends on E_k and ϵ_e (the electron equipartition parameter). Furthermore, the fraction of energy in the electrons (ϵ_e) is quite centered around 0.1, based on the large-sample afterglow analysis. Thus, E_k can be well estimated by the $L_{X,11\text{h}}$ as following (Lloyd-Ronning & Zhang 2004):

$$\begin{aligned} E_k &= 10^{52} \text{ ergs R} \left[\frac{L_{X,10\text{h}}}{10^{46} \text{ ergs s}^{-1}} \right]^{4/(2+p)} \left(\frac{1+z}{2} \right)^{-1} \\ &\times \epsilon_{e,-1}^{4(1-p)/(2+p)} \epsilon_{B,-2}^{(2-p)/(2+p)} t_{10\text{h}}^{(3p-2)/(2+p)} \nu_{18}^{2(p-2)/(2+p)} \\ &\simeq 10^{52} \text{ ergs R} \left[\frac{1.1 L_{X,11\text{h}}}{10^{46} \text{ ergs s}^{-1}} \right] \left(\frac{1+z}{2} \right)^{-1} \\ &\times (\epsilon_{e,-1})^{-1}, \quad (p \simeq 2) \end{aligned} \quad (19)$$

where $R = [t(10 \text{ h})/t(\text{prompt})]^{(17/16)\epsilon_e} \sim 2.27$ is the radiative losses during the first 10 hours after the prompt phase. Note that the derived E_k is 9.2 times larger in Fan & Piran (2006), since the ν_m (the characteristic frequency corresponding to the minimum electron Lorentz

factor) is about one and a half orders smaller. Previously, it had been hard to judge which constant was better. Here, using the method ($\epsilon_\gamma = 50\%$ and the maximum Γ ; see Section 4.1) in this work, our result ($E_{k,52} \simeq 3.7 * L_{X,45}$) is quite consistent with $E_{k,52} \simeq 2.5 * L_{X,45}$ (Fan & Piran 2006, without the inverse Compton effect).

The isotropic X-ray afterglow luminosity (in the 2-10 keV rest-frame common energy band) at 11 hours (rest frame), $L_{X,11\text{h}}$, is computed from the observed integral 0.3-10 keV unabsorbed fluxes at 11 hours ($F_{X,11\text{h}}$; estimated from the *Swift*/XRT light curves) and the measured spectral index Γ_1 (from the XRT spectra), along with the luminosity distance D_L . The equation is as follows (D'Avanzo et al. 2012):

$$\begin{aligned} L_{X,11\text{h}}(2 - 10 \text{ keV}) &= 4\pi D_L^2 \cdot F_{X,11\text{h}}(0.3 - 10 \text{ keV}) \cdot \\ &\frac{\left(\frac{10}{1+z}\right)^{2-\Gamma_1} - \left(\frac{2}{1+z}\right)^{2-\Gamma_1}}{10^{2-\Gamma_1} - 0.3^{2-\Gamma_1}}. \end{aligned} \quad (20)$$

Here, $F_{X,11\text{h}}$ is obtained by interpolating (or extrapolating) the best-fit power law, for the XRT light curve within a selected time range including (or close to) 11 hours, to the 11 hours.

B.2. THE POWER-LAW SHAPE OF THE X-RAY AFTERGLOW PREDICTED BY THE CLASSICAL HOT FIREBALL.

The ‘‘generic’’ afterglow model (relativistic blast-wave theory) for GRB predicts a power-law decaying multi-wavelength afterglow (Paczynski & Rhoads 1993; Mészáros & Rees 1997), due to the self-similar nature of the blastwave solution. The observed specific flux is

$$\begin{aligned} f_\nu &\propto E_k^{(p+2)/4} \epsilon_e^{p-1} \epsilon_B^{(p-2)/4} t_{\text{obs}}^{-(3p-2)/4} \nu^{-p/2} \\ &\simeq \frac{(\epsilon_e E_k)}{t_{\text{obs}}} \nu^{-1}, \quad (p \simeq 2). \end{aligned} \quad (21)$$

This power-law behavior ($f \sim t_{\text{obs}}^{-1}$) is well consistent with the observations of the optical and radio afterglows. But several surprising emission components (the steep decay $f \sim t_{\text{obs}}^{-3}$ phase, the plateau $f \sim t_{\text{obs}}^{-0.5}$ phase, and the flare) in the early X-ray afterglow are revealed by the *Swift* observations (Zhang et al. 2006), which are not predicted by the above standard (hot fireball) model. These extra components imply that an extra energy injection (internal or external) may exist, which can be magnetic-dominated.

B.3. THE REVERSE SHOCK IN THE OPTICAL AFTERGLOW PREDICTED BY THE CLASSICAL HOT FIREBALL.

For the classical hot fireball (the magnetic field in the ejecta is dynamically unimportant, namely the magnetization parameter $\sigma \equiv B'^2/(4\pi n'_p m_p c^2) \ll 1$), a strong reverse shock (propagating back across the GRB ejecta to decelerate it) is predicted in the early optical afterglow phase (Mészáros & Rees 1997; Sari & Piran 1999). This prediction is almost confirmed by the discovery of a very bright optical flash in GRB 990123 while the GRB is still active. Later on, many more reverse shock signals are found. The light curve of the reverse shock declines more rapidly ($f \sim t^{-2}$) than that of the forward shock ($f \sim t^{-1}$), and rises more rapidly ($f \gtrsim t^3$) than that of the forward shock ($f \sim t^2$) before the peak time.

B.4. THE *FERMI*/LAT (GEV EMISSION) LIGHT CURVE FROM THE RADIATIVE FIREBALL.

For the generic afterglow model, the total energy of the fireball remains constant (the adiabatic case) after the forward shock starts to decelerate (entering the self-similar phase). However, there could be another case that the total energy of the fireball decreases (the radiative case), since a large fraction of the dissipated energy

is radiated away (by magnetic reconnection or electron-proton collisions) (Ghisellini et al. 2010). For this radiative fireball, the light curve (after the peak time) declines more rapidly ($f \sim t^{-10/7}$), $\Gamma \propto t^{-3/7}$ ($\Gamma \propto t^{-3/8}$ for the adiabatic case), and the peak time is much earlier ($t_{\text{peak}} = 0.44t_{\text{dec}}$, $t_{\text{peak}} = 0.63t_{\text{dec}}$ for the adiabatic case; t_{dec} is the deceleration time).

REFERENCES

- Abdo, A. A., Ackermann, M., Ajello, M., et al. 2009, *ApJ*, 706, L138
- Abramowicz, M. A., Novikov, I. D., & Paczynski, B. 1991, *ApJ*, 369, 175
- Acuner, Z., & Ryde, F. 2018, *MNRAS*, 475, 1708
- Acuner, Z., Ryde, F., Pe'er, A., et al. 2020, *ApJ*, 893, 128
- Amati, L., Frontera, F., Tavani, M., et al. 2002, *A&A*, 390, 81
- Axelsson, M., Baldini, L., Barbiellini, G., et al. 2012, *ApJ*, 757, L31
- Axelsson, M., & Borgonovo, L. 2015, *MNRAS*, 447, 3150
- Band, D., Matteson, J., Ford, L., et al. 1993, *ApJ*, 413, 281
- Bégué, D., & Pe'er, A. 2015, *ApJ*, 802, 134
- Beloborodov, A. M. 2011, *ApJ*, 737, 68
- Beloborodov, A. M. 2017, *ApJ*, 838, 125
- Bhattacharya, M., Lu, W., Kumar, P., et al. 2018, *ApJ*, 852, 24
- Bhattacharya, M. & Kumar, P. 2020, *MNRAS*, 491, 4656
- Burgess, J. M., Greiner, J., Bégué, D., & Berlato, F. 2017, arXiv:1710.08362
- Burgess, J. M., Bégué, D., Greiner, J., et al. 2020, *Nature Astronomy*, 4, 174
- Dai, Z. G., & Gou, L. J. 2001, *ApJ*, 552, 72
- D'Avanzo, P., Salvaterra, R., Sbarufatti, B., et al. 2012, *MNRAS*, 425, 506
- Deng, L.-T., Lin, D.-B., Zhou, L., et al. 2022, *ApJ*, 934, L22
- Deng, W., & Zhang, B. 2014, *ApJ*, 785, 112
- Dereli-Bégué, H., Pe'er, A., & Ryde, F. 2020, *ApJ*, 897, 145
- Fan, Y., & Piran, T. 2006, *MNRAS*, 369, 197
- Fan, Y.-Z., Wei, D.-M., Zhang, F.-W., & Zhang, B.-B. 2012, *ApJ*, 755, L6
- Gao, H., Wang, X.-G., Mészáros, P., et al. 2015, *ApJ*, 810, 160
- Geng, J.-J., Huang, Y.-F., Wu, X.-F., Zhang, B., & Zong, H.-S. 2018, *ApJS*, 234, 3
- Geng, J.-J., Zhang, B., Kölligan, A., Kuiper, R., & Huang, Y.-F. 2019, *ApJ*, 877, L40
- Ghirlanda, G., Nava, L., Ghisellini, G., et al. 2012, *MNRAS*, 420, 483
- Ghirlanda, G., Pescalli, A., & Ghisellini, G. 2013, *MNRAS*, 432, 3237
- Ghirlanda, G., Nappo, F., Ghisellini, G., et al. 2018, *A&A*, 609, A112
- Ghisellini, G., Ghirlanda, G., Nava, L., et al. 2010, *MNRAS*, 403, 926
- Giannios, D. & Spruit, H. C. 2007, *A&A*, 469, 1
- Goldstein, A., Burgess, J. M., Preece, R. D., et al. 2012, *ApJS*, 199, 19
- Gompertz, B. P., Levan, A. J., & Tanvir, N. R. 2020, *ApJ*, 895, 58
- Goodman, J. 1986, *ApJ*, 308, L47
- Gruber, D., Goldstein, A., Weller von Ahlefeld, V., et al. 2014, *ApJS*, 211, 12
- Guiriec, S., Connaughton, V., Briggs, M. S., et al. 2011, *ApJ*, 727, L33
- Guiriec, S., Daigne, F., Hascot, R., et al. 2013, *ApJ*, 770, 32
- Hou, S.-J., Zhang, B.-B., Meng, Y.-Z., et al. 2018, *ApJ*, 866, 13
- Iyyani, S. & Sharma, V. 2021, *ApJS*, 255, 25
- Kaneko, Y., Preece, R. D., Briggs, M. S., et al. 2006, *ApJS*, 166, 298
- Kobayashi, S., Piran, T., & Sari, R. 1997, *ApJ*, 490, 92
- Lan, L., Lu, R.-J., Lü, H.-J., et al. 2020, *MNRAS*, 492, 3622
- Larsson, J., Racusin, J. L., & Burgess, J. M. 2015, *ApJ*, 800, L34
- Lazzati, D., Morsony, B. J., Margutti, R., & Begelman, M. C. 2013, *ApJ*, 765, 103
- Li, L., Liang, E.-W., Tang, Q.-W., et al. 2012, *ApJ*, 758, 27
- Li, L., Wang, Y., Shao, L., et al. 2018, *ApJS*, 234, 26
- Li, L. 2019a, *ApJS*, 242, 16
- Li, L., Geng, J.-J., Meng, Y.-Z., et al. 2019b, *ApJ*, 884, 109
- Li, L. 2019c, *ApJS*, 245, 7
- Li, L. 2020, *ApJ*, 894, 100
- Li, L., Ryde, F., Pe'er, A., et al. 2021, *ApJS*, 254, 35
- Liang, E., & Kargatis, V. 1996, *Nature*, 381, 49
- Liang, E.-W., Li, L., Gao, H., et al. 2013, *ApJ*, 774, 13
- Liang, E.-W., Lin, T.-T., Lü, J., et al. 2015, *ApJ*, 813, 116
- Lin, D.-B., Liu, T., Lin, J., et al. 2018, *ApJ*, 856, 90
- Lloyd-Ronning, N. M., & Zhang, B. 2004, *ApJ*, 613, 477
- Lu, R.-J., Hou, S.-J., & Liang, E.-W. 2010, *ApJ*, 720, 1146
- Lu, R.-J., Wei, J.-J., Liang, E.-W., et al. 2012, *ApJ*, 756, 112
- Lundman, C., Pe'er, A., & Ryde, F. 2013, *MNRAS*, 428, 2430
- Lü, J., Zou, Y.-C., Lei, W.-H., et al. 2012, *ApJ*, 751, 49
- Meng, Y.-Z., Geng, J.-J., Zhang, B.-B., et al. 2018, *ApJ*, 860, 72
- Meng, Y.-Z., Liu, L.-D., Wei, J.-J., Wu, X.-F., & Zhang, B.-B. 2019, *ApJ*, 882, 26
- Meng, Y.-Z., Geng, J.-J., & Wu, X.-F. 2022, *MNRAS*, 509, 6047
- Mészáros, P. & Rees, M. J. 1997, *ApJ*, 476, 232
- Mészáros, P., & Rees, M. J. 2000, *ApJ*, 530, 292
- Mészáros, P. 2002, *ARA&A*, 40, 137
- Minaev, P. Y. & Pozanenko, A. S. 2020, *MNRAS*, 492, 1919
- Nava, L., Salvaterra, R., Ghirlanda, G., et al. 2012, *MNRAS*, 421, 1256
- Paczynski, B. 1986, *ApJ*, 308, L43
- Paczynski, B. & Rhoads, J. E. 1993, *ApJ*, 418, L5
- Parsotan, T. & Lazzati, D. 2022, *ApJ*, 926, 104
- Pe'er, A. 2008, *ApJ*, 682, 463
- Pe'er, A., & Ryde, F. 2011, *ApJ*, 732, 49
- Pe'er, A., Barlow, H., O'Mahony, S., et al. 2015, *ApJ*, 813, 127
- Piran, T. 1999, *Phys. Rep.*, 314, 575
- Rees, M. J., & Meszaros, P. 1994, *ApJ*, 430, L93
- Rees, M. J., & Mészáros, P. 2005, *ApJ*, 628, 847
- Rossi, E., Lazzati, D., & Rees, M. J. 2002, *MNRAS*, 332, 945
- Ruffini, R., Siutsou, I. A., & Vereshchagin, G. V. 2013, *ApJ*, 772, 11
- Ryde, F. 2004, *ApJ*, 614, 827
- Ryde, F. 2005, *ApJ*, 625, L95
- Ryde, F., & Pe'er, A. 2009, *ApJ*, 702, 1211
- Ryde, F., Axelsson, M., Zhang, B. B., et al. 2010, *ApJ*, 709, L172
- Ryde, F., Lundman, C., & Acuner, Z. 2017, *MNRAS*, 472, 1897
- Sari, R. & Piran, T. 1999, *ApJ*, 520, 641
- Song, X.-Y. & Meng, Y.-Z. 2022, *MNRAS*, 512, 5693
- Tang, Q.-W., Wang, K., Li, L., et al. 2021, *ApJ*, 922, 255
- Thompson, C. 1994, *MNRAS*, 270, 480
- Tsvetkova, A., Frederiks, D., Golenetskii, S., et al. 2017, *ApJ*, 850, 161
- Uhm, Z. L. & Zhang, B. 2014, *Nature Physics*, 10, 351
- Vereshchagin, G. V. & Siutsou, I. A. 2020, *MNRAS*, 494, 1463
- Vereshchagin, G., Li, L., & Bégué, D. 2022, *MNRAS*, 512, 4846
- von Kienlin, A., Meegan, C. A., Paciesas, W. S., et al. 2020, *ApJ*, 893, 46
- Vurm, I., & Beloborodov, A. M. 2016, *ApJ*, 831, 175
- Vyas, M. K., Pe'er, A., & Eichler, D. 2021, *ApJ*, 908, 9
- Wang, K., Lin, D.-B., Wang, Y., et al. 2020, *ApJ*, 899, 111
- Wang, Y., Zheng, T.-C., & Jin, Z.-P. 2022, arXiv:2205.08427
- Wygoda, N., Guetta, D., Mandich, M. A., & Waxman, E. 2016, *ApJ*, 824, 127
- Xue, L., Zhang, F.-W., & Zhu, S.-Y. 2019, *ApJ*, 876, 77
- Yamazaki, R., Sato, Y., Sakamoto, T., et al. 2020, *MNRAS*, 494, 5259
- Yang, J., Chand, V., Zhang, B.-B., et al. 2020, *ApJ*, 899, 106
- Yi, S.-X., Wu, X.-F., Zou, Y.-C., et al. 2020, *ApJ*, 895, 94
- Yu, H.-F., van Eerten, H. J., Greiner, J., et al. 2015, *A&A*, 583, A129

- Yu, H.-F., Preece, R. D., Greiner, J., et al. 2016, *A&A*, 588, A135
- Zhang, B., & Mészáros, P. 2002a, *ApJ*, 571, 876
- Zhang, B., Fan, Y. Z., Dyks, J., et al. 2006, *ApJ*, 642, 354
- Zhang, B., Liang, E., Page, K. L., et al. 2007, *ApJ*, 655, 989
- Zhang, B. 2011, *Comptes Rendus Physique*, 12, 206
- Zhang, B., & Yan, H. 2011, *ApJ*, 726, 90
- Zhang, B. 2020, *Nature Astronomy*, 4, 210
- Zhang, B.-B., Zhang, B., Liang, E.-W., et al. 2011, *ApJ*, 730, 141
- Zhang, B.-B., Zhang, B., Castro-Tirado, A. J., et al. 2018a, *Nature Astronomy*, 2, 69
- Zhang, B.-B., Zhang, B., Sun, H., et al. 2018b, *Nature Communications*, 9, 447
- Zhang, B.-B., Liu, Z.-K., Peng, Z.-K., et al. 2021, *Nature Astronomy*, 5, 91
- Zhang, Z. J., Zhang, B.-B., & Meng, Y.-Z. 2021, arXiv:2109.14252
- Zhao, P.-W., Tang, Q.-W., Zou, Y.-C., et al. 2022, *ApJ*, 929, 179

TABLE 2
THE OBSERVED QUANTITIES AND INFERRED EFFICIENCY FOR THE $\epsilon_\gamma \lesssim 50\%$ SUB-SAMPLE AFTER GRB 110213A.

| $\epsilon_\gamma \lesssim 50\%$ sub-sample (62 bursts) | | | | | | | | | |
|--|--------|---------------------|--------------------------------------|---|---|--------------------|------------------------------|----------|-----------------|
| GRB | z | $E_{p,z}$ (keV) | E_{iso} (10^{52} erg) | $L_{X,11}$ (10^{45} erg s $^{-1}$) | $E_{\text{iso}}/[\frac{3.7*L_{X,11}}{(1+z)^2}]$ | E_{ratio} | $(R_{\text{ph}}/R_s)^{-2/3}$ | Γ | $T_{90,i}$ s |
| 110213A | 1.46 | 183.83 \pm 32.15 | 6.9 | 3.22 | 0.713 | 0.225 | 0.283 | 157 | 11.9 |
| 110213B | 1.083 | 256 \pm 40 | 7.04 | 3.66 | 0.541 | 0.348 | | | |
| 110715A | 0.82 | 216.58 \pm 12.74 | 4.97 | 9.99 | 0.122 | 0.313 | | | |
| 111209A | 0.677 | 520 \pm 89 | 5.2 | 2.95 | 0.399 | 0.991 | | | |
| 111228A | 0.7156 | 74 \pm 53 | 1.65 | 3.24 | 0.118 | 0.056 | | | |
| 120326A | 1.798 | 115 \pm 19 | 3.82 | 15.6 | 0.093 | 0.147 | | | |
| 120804A | 1.3 | 283 \pm 62 | 0.657 | 1.09 | 0.187 | 0.877 | | | |
| 120811C | 2.671 | 203.98 \pm 19.55 | 8.81 | 7.25 | 0.603 | 0.239 | | | |
| 120907A | 0.97 | 241.16 \pm 67.27 | 0.18 | 1.02 | 0.047 | 1.09 | | | |
| 121211A | 1.023 | 202.76 \pm 32.05 | 0.14 | 2.54 | 0.015 | 0.942 | | | |
| 130420A | 1.297 | 131.59 \pm 7.2 | 6.29 | 2.99 | 0.653 | 0.149 | 0.644 | 149 | 45.7 |
| 130612A | 2.006 | 186 \pm 32 | 0.719 | 0.32 | 0.913 | 0.487 | 0.653 | 193 | 1.9 |
| 130701A | 1.16 | 192.24 \pm 8.64 | 2.62 | 1.32 | 0.580 | 0.33 | | | |
| 130702A | 0.145 | 17.2 \pm 5.7 | 0.064 | 1.01 | 0.010 | 0.028 | | | |
| 130831A | 0.48 | 81.4 \pm 13.32 | 0.805 | 1.02 | 0.157 | 0.156 | 0.154 | 73 | 11.9 |
| 130925A | 0.347 | 110.94 \pm 3.1 | 15. | 14.6 | 0.187 | 0.089 | | | |
| 131117A | 4.042 | 222 \pm 37 | 1.03 | 1.43 | 0.491 | 0.546 | | | |
| 131231A | 0.6439 | 292.52 \pm 6.06 | 21.1 | 13. | 0.361 | 0.288 | 0.142 | 145 | 17.7 |
| 140213A | 1.2076 | 191.24 \pm 7.85 | 8.88 | 13.4 | 0.197 | 0.218 | | | |
| 140226A | 1.98 | 1234 \pm 235 | 5.68 | 1.71 | 1.340 | 3.05 | | | |
| 140304A | 5.283 | 775.06 \pm 173.37 | 10.3 | 5.19 | 1.690 | 1.34 | | | |
| 140506A | 0.889 | 373.19 \pm 61.49 | 1.4 | 5.88 | 0.060 | 0.986 | | | |
| 140508A | 1.027 | 533.46 \pm 28.44 | 22.5 | 14.4 | 0.428 | 0.629 | | | |
| 140512A | 0.72 | 826 \pm 201.24 | 7.25 | 6.98 | 0.241 | 2.64 | | | |
| 140515A | 6.32 | 376 \pm 108 | 5.38 | 3.15 | 1.690 | 0.636 | | | |
| 140606B | 0.384 | 352 \pm 46 | 0.25 | 1. | 0.047 | 1.62 | | | |
| 140620A | 2.04 | 230.19 \pm 33.87 | 7.28 | 11.4 | 0.263 | 0.299 | | | |
| 140801A | 1.32 | 250.6 \pm 7. | 5.55 | 1.87 | 0.930 | 0.366 | | | |
| 140907A | 1.21 | 313 \pm 21 | 2.71 | 3.58 | 0.226 | 0.626 | | | |
| 141109A | 2.993 | 763 \pm 303 | 33.1 | 10. | 1.780 | 0.891 | | | |
| 141221A | 1.452 | 450.62 \pm 87.15 | 2.46 | 1.11 | 0.734 | 1.05 | 0.965 | 202 | 9.7 |
| 141225A | 0.915 | 342.71 \pm 52.13 | 0.859 | 0.494 | 0.450 | 1.04 | | | |
| 150206A | 2.09 | 704.52 \pm 71.07 | 61.9 | 21.1 | 1.220 | 0.651 | | | |
| 150301B | 1.5169 | 460.51 \pm 90.95 | 1.99 | 0.567 | 1.190 | 1.16 | | | |
| 150323A | 0.59 | 151.05 \pm 14.31 | 1.26 | 0.427 | 0.632 | 0.306 | | | |
| 150403A | 2.06 | 1311.74 \pm 53.09 | 116. | 43.9 | 1.100 | 1.21 | | | |
| 150514A | 0.807 | 116.72 \pm 10.19 | 0.878 | 1.26 | 0.171 | 0.245 | | | |
| 150727A | 0.313 | 195.05 \pm 25.18 | 0.2 | 0.062 | 0.575 | 0.794 | | | |
| 150818A | 0.282 | 128 \pm 37 | 0.1 | 0.09 | 0.193 | 0.571 | | | |
| 151027A | 0.81 | 366.76 \pm 61.78 | 3.3 | 6.17 | 0.131 | 0.724 | | | |
| 151029A | 1.423 | 82 \pm 17 | 0.288 | 0.232 | 0.407 | 0.221 | | | |
| 160227A | 2.38 | 222 \pm 55 | 5.56 | 14.6 | 0.174 | 0.311 | | | |
| 160509A | 1.17 | 770.74 \pm 20.82 | 113. | 37.8 | 0.877 | 0.6 | | | |
| 160623A | 0.37 | 756.24 \pm 19.18 | 25.3 | 14.8 | 0.317 | 0.963 | | | |
| 160804A | 0.736 | 123.93 \pm 7.25 | 2.7 | 1.16 | 0.543 | 0.182 | | | |
| 161017A | 2.013 | 718.83 \pm 122.83 | 8.3 | 4.35 | 0.777 | 1.31 | | | |
| 161117A | 1.549 | 205.62 \pm 7.76 | 13. | 7.04 | 0.637 | 0.212 | | | |
| 161219B | 0.1475 | 71. \pm 19.3 | 0.012 | 0.778 | 0.002 | 0.533 | | | |
| 170113A | 1.968 | 333.92 \pm 174.49 | 0.924 | 6. | 0.061 | 0.976 | | | |
| 170604A | 1.329 | 512 \pm 168 | 4.7 | 4.61 | 0.321 | 1. | | | |
| 170607A | 0.557 | 174.06 \pm 14.06 | 0.915 | 3.1 | 0.062 | 0.411 | | | |
| 170705A | 2.01 | 294.61 \pm 23.01 | 18. | 25.3 | 0.289 | 0.307 | | | |
| 170903A | 0.886 | 180 \pm 25 | 0.865 | 3.02 | 0.073 | 0.438 | | | |
| 171205A | 0.0368 | 125 $^{+141}_{-37}$ | 0.002 | 0.003 | 0.116 | 1.98 | | | |
| 171222A | 2.409 | 694 \pm 12 | 8.94 | 5.83 | 0.706 | 1.22 | | | |
| 180205A | 1.409 | 205 \pm 34 | 0.972 | 1.63 | 0.194 | 0.501 | | | |
| 180620B | 1.1175 | 372 \pm 105 | 3.04 | 12.4 | 0.070 | 0.758 | | | |
| 180720B | 0.654 | 1052 \pm 26 | 34. | 32. | 0.237 | 1.36 | | | |
| 180728A | 0.117 | 108 \pm 8 | 0.233 | 1.11 | 0.032 | 0.343 | | | |
| 181201A | 0.45 | 220 \pm 9 | 10. | 11.7 | 0.168 | 0.253 | | | |
| 190106A | 1.859 | 489 \pm 257 | 9.96 | 14.1 | 0.272 | 0.735 | | | |
| 190114C | 0.4245 | 929.3 \pm 9.4 | 27. | 9.3 | 0.560 | 1.24 | | | |

TABLE 3
 THE OBSERVED QUANTITIES AND INFERRED EFFICIENCY FOR THE $\epsilon_\gamma \gtrsim 50\%$ SUB-SAMPLE AFTER GRB 110213A.

| GRB | z | $\epsilon_\gamma \gtrsim 50\%$ sub-sample (40 bursts) | | | | | η/Γ | Γ | L_{iso} (10^{52} erg s $^{-1}$) |
|---------|--------|---|--------------------------------------|---|---|-------|---------------|----------|---|
| | | $E_{p,z}$ (keV) | E_{iso} (10^{52} erg) | $L_{X,11}$ (10^{45} erg s $^{-1}$) | $E_{\text{iso}}/[\frac{3.7*L_{X,11}}{(1+z)^2}]$ | | | | |
| 110422A | 1.77 | 429.35 \pm 8.31 | 74.700 | 5.450 | 5.140 | | | | |
| 110503A | 1.61 | 574.2 \pm 31.32 | 21.300 | 4.390 | 1.710 | | | | |
| 110731A | 2.83 | 1223 \pm 75.4 | 31.500 | 4.650 | 3.510 | 1.722 | 500 | 20.52 | |
| 110918A | 0.98 | 665.28 \pm 79.2 | 271.000 | 39.100 | 1.850 | | | | |
| 111008A | 5. | 624 \pm 186 | 41.400 | 9.390 | 3.580 | | | | |
| 120119A | 1.728 | 499.91 \pm 21.71 | 40.200 | 4.100 | 3.610 | | | | |
| 120711A | 1.405 | 2552 \pm 91 | 204.000 | 39.800 | 1.660 | 7.587 | 258 | 14.37 | |
| 120712A | 4.1745 | 642 \pm 134.5 | 15.200 | 2.310 | 4.600 | | | | |
| 120909A | 3.93 | 961.41 \pm 125.42 | 69.000 | 7.570 | 6.070 | 5.060 | 288 | 14.88 | |
| 121128A | 2.2 | 244.19 \pm 9.61 | 10.100 | 1.000 | 4.340 | 3.891 | 332 | 6.64 | |
| 130408A | 3.76 | 1289.96 \pm 204.68 | 32.400 | 5.570 | 3.740 | | | | |
| 130427A | 0.34 | 1105.4 \pm 7.3 | 89.000 | 17.000 | 0.947 | 1.050 | 471 | 11.86 | |
| 130505A | 2.27 | 1939.11 \pm 85.02 | 438.000 | 29.400 | 6.590 | | | | |
| 130514A | 3.6 | 506 \pm 193 | 49.500 | 5.730 | 5.370 | | | | |
| 130518A | 2.488 | 1388.34 \pm 55.23 | 216.000 | 6.000 | 17.000 | | | | |
| 130610A | 2.092 | 840.81 \pm 344.98 | 5.780 | 0.645 | 3.750 | 6.465 | 204 | 1.3 | |
| 130907A | 1.24 | 866.88 \pm 35.84 | 385.000 | 23.900 | 4.870 | | | | |
| 131030A | 1.29 | 448.84 \pm 13.74 | 32.700 | 7.060 | 1.430 | | | | |
| 131105A | 1.686 | 713.18 \pm 46.18 | 15.300 | 3.340 | 1.660 | | | | |
| 140206A | 2.73 | 1780.44 \pm 119.77 | 278.000 | 26.800 | 5.220 | | | | |
| 140419A | 3.96 | 1398.72 \pm 188.48 | 228.000 | 10.800 | 14.200 | | | | |
| 140423A | 3.26 | 516.74 \pm 64.73 | 43.800 | 4.720 | 5.350 | 6.019 | 303 | 6.05 | |
| 140629A | 2.275 | 282 \pm 56 | 4.400 | 0.575 | 3.390 | | | | |
| 140703A | 3.14 | 861.25 \pm 148.3 | 18.400 | 3.280 | 3.130 | | | | |
| 141004A | 0.573 | 231 \pm 44 | 0.210 | 0.051 | 0.877 | | | | |
| 141028A | 2.33 | 979.59 \pm 53.39 | 51.000 | 7.460 | 3.070 | | | | |
| 141220A | 1.3195 | 418.8 \pm 24.17 | 2.290 | 0.322 | 2.230 | | | | |
| 150314A | 1.758 | 957.28 \pm 19.06 | 76.800 | 5.090 | 5.620 | | | | |
| 151021A | 2.33 | 566.1 \pm 43.29 | 113.000 | 4.470 | 11.400 | | | | |
| 160131A | 0.97 | 1282.47 \pm 453.1 | 87.000 | 6.990 | 3.310 | | | | |
| 160625B | 1.406 | 1134.34 \pm 15.51 | 510.000 | 39.200 | 4.230 | | | | |
| 161023A | 2.708 | 604.4 \pm 137.2 | 68.000 | 5.900 | 5.780 | | | | |
| 161129A | 0.645 | 240.84 \pm 70.09 | 0.783 | 0.059 | 2.970 | | | | |
| 170202A | 3.645 | 1147 \pm 771 | 17.000 | 4.420 | 2.410 | | | | |
| 171010A | 0.3285 | 227.17 \pm 9.3 | 18.000 | 2.880 | 1.123 | | | | |
| 180325A | 2.248 | 993.89 \pm 162.4 | 23.000 | 1.300 | 7.770 | | | | |
| 180329B | 1.998 | 146 \pm 28 | 4.690 | 0.995 | 1.910 | | | | |
| 180914B | 1.096 | 977 \pm 61 | 370.000 | 7.600 | 13.800 | | | | |
| 181020A | 2.938 | 1461 \pm 225 | 82.800 | 4.560 | 9.660 | | | | |
| 181110A | 1.505 | 120 \pm 68 | 11.000 | 0.937 | 3.970 | | | | |

TABLE 4
FITTING RESULTS OF THE TIME-INTEGRATED SPECTRUM FOR THE BURSTS WITH EXTREMELY HIGH EFFICIENCY (DETECTED BY *Fermi*)

| GRB | α (CPL) | E_c (CPL) | F (CPL) | α (Band) | β (Band) | E_p (Band) | F (Band) | ΔDIC (Band-CPL) | p_{DIC} (CPL) | p_{DIC} (Band) |
|---------|-------------------------|---------------------|---------------------------------------|-------------------------|-------------------------|-------------------|---------------------------------------|----------------------------------|---------------------------|----------------------------|
| 110818A | $-1.18^{+0.15}_{-0.15}$ | 352^{+169}_{-161} | $0.18^{+0.12}_{-0.06} \times 10^{-6}$ | $0.48^{+0.50}_{-0.56}$ | $-1.70^{+0.07}_{-0.07}$ | 42^{+7}_{-7} | $0.46^{+1.54}_{-0.35} \times 10^{-6}$ | -141.4 | -2.9 | -151.3 |
| 120729A | $-0.55^{+0.04}_{-0.04}$ | 163^{+23}_{-24} | $0.17^{+0.05}_{-0.04} \times 10^{-6}$ | $-0.55^{+0.04}_{-0.04}$ | $-4.93^{+2.44}_{-2.66}$ | 229^{+30}_{-29} | $0.19^{+0.07}_{-0.04} \times 10^{-6}$ | -1.3 | 1.9 | 1.4 |
| 131108A | $-0.93^{+0.02}_{-0.02}$ | 380^{+25}_{-26} | $1.36^{+0.12}_{-0.10} \times 10^{-6}$ | $0.66^{+0.08}_{-0.08}$ | $-1.60^{+0.01}_{-0.01}$ | 61^{+0}_{-0} | $3.54^{+0.69}_{-0.61} \times 10^{-6}$ | 599.9 | 2.9 | 1.7 |
| 150821A | $-1.19^{+0.02}_{-0.02}$ | 419^{+35}_{-35} | $0.64^{+0.05}_{-0.05} \times 10^{-6}$ | $-1.18^{+0.03}_{-0.03}$ | $-3.87^{+1.71}_{-3.16}$ | 313^{+31}_{-32} | $0.76^{+0.19}_{-0.15} \times 10^{-6}$ | -8.0 | 2.9 | -1.5 |
| 161014A | $-0.74^{+0.10}_{-0.10}$ | 144^{+24}_{-24} | $0.22^{+0.07}_{-0.05} \times 10^{-6}$ | $1.52^{+0.34}_{-0.34}$ | $-1.74^{+0.04}_{-0.04}$ | 48^{+2}_{-2} | $0.63^{+0.82}_{-0.37} \times 10^{-6}$ | 3.0 | 1.6 | -40.0 |
| 170214A | $-1.06^{+0.01}_{-0.01}$ | 570^{+26}_{-26} | $1.53^{+0.08}_{-0.06} \times 10^{-6}$ | $-1.05^{+0.01}_{-0.01}$ | $-2.77^{+0.36}_{-0.12}$ | 510^{+22}_{-22} | $1.81^{+0.15}_{-0.14} \times 10^{-6}$ | -10.6 | 3.0 | 2.7 |

Note—For 120729A, 150821A and 170214A, the high-energy spectral indices for BAND function are very small (-4.93, -3.87 and -2.77), while the low-energy spectral indices and peak energy for BAND function and CPL model are very similar. For 110818A, 131108A and 161014A, the low-energy spectral indices for BAND function are extremely hard (0.48, 0.66, 1.52), and the peak energy is extremely small (42, 61, 48). Thus, the CPL model is surely the best-fit model.

TABLE 5
THE BURSTS WITH ALMOST SAME E_{RATIO} AND E_{ISO}/E_k ($\epsilon_\gamma \lesssim 50\%$) AND THEIR POWER-LAW SLOPE OF THE X-RAY AFTERGLOW LIGHT CURVE.

| Bursts after GRB 110213A | | | | Bursts before GRB 110213A | | | |
|--------------------------|---|--------------------|-------------|---------------------------|---|--------------------|-------------|
| GRB | $E_{\text{iso}}/[\frac{3.7 * L_{X,11}}{(1+z)^2}]$ | E_{ratio} | X-ray slope | GRB | $E_{\text{iso}}/[\frac{3.7 * L_{X,11}}{(1+z)^2}]$ | E_{ratio} | X-ray slope |
| 130420A | 0.653 | 0.644 ^a | -0.900 | 050922C | 0.898 | 0.821 | -1.200 |
| 130831A | 0.157 | 0.156 | -0.959 | 060210 | 0.751 | 0.597 | -0.970 |
| 131117A | 0.491 | 0.546 | -0.998 | 060306 | 0.567 | 0.435 | -1.047 |
| 140213A | 0.197 | 0.218 | -1.070 | 080603B | 0.629 | 0.528 | -0.850 |
| 150301B | 1.190 | 1.16 | -1.179 | 091018 | 0.112 | 0.092 | -1.160 |
| 150403A | 1.100 | 1.21 | -1.140 | 091020 | 0.912 | 0.831 | -1.090 |
| 170705A | 0.289 | 0.307 | -0.969 | 100621A | 0.159 | 0.193 | -0.987 |

^a $E_{\text{iso}}/E_k = (R_{\text{ph}}/R_s)^{-2/3}$

TABLE 6
 THE OBSERVED QUANTITIES, INFERRED EFFICIENCY (E_{RATIO} AND $(R_{\text{PH}}/R_s)^{-2/3}$) AND INFERRED Γ (FROM $T_{p,op}$ AND PROMPT EMISSION) FOR THE BURSTS WITH $T_{p,op}$ DETECTION.

| $\epsilon_\gamma \lesssim 50\%$ sub-sample (24 bursts) | | | | | | | | | | | | |
|--|------|--------------------|---------------------|--------------------------------------|--------------------|------------------------------|-----------------|-----------------|---------------|------------|------------|---|
| GRB | z | $dE_{p,z}/E_{p,z}$ | $E_{p,z}$ (keV) | E_{iso} (10^{52} erg) | E_{ratio} | $(R_{\text{ph}}/R_s)^{-2/3}$ | $T_{90,i}$ s | $T_{p,op}$ s | Γ_{op} | Γ_E | Γ_L | L_{iso} (10^{52} erg s $^{-1}$) |
| $dE_{p,z}/E_{p,z} \lesssim 0.2$ | | | | | | | | | | | | |
| 060124 | 2.3 | 0.176 | 635.0 \pm 112.0 | 43.000 | 0.640 | 0.362 | 72.2 | 631.0 | 220.0 | 272.0 | 451.0 | 14.200 |
| 090618 | 0.54 | 0.059 | 156.0 \pm 9.2 | 25.300 | 0.267 | 0.710 | 67.7 | 91.2 | 319.0 | 128.0 | 340.0 | 2.050 |
| 090926A | 2.11 | 0.028 | 908.0 \pm 25.0 | 200.000 | 0.617 | 0.732 | 4.3 | 8.1 | 851.0 | 798.0 | 828.0 | 74.000 |
| 091020 | 1.71 | 0.037 | 507.0 \pm 19.0 | 7.910 | 0.833 | 0.689 | 10.8 | 135.0 | 295.0 | 316.0 | 254.0 | 3.300 |
| 100728B | 2.11 | 0.116 | 404.0 \pm 47.0 | 7.240 | 0.716 | 1.230 | 3.9 | 33.9 | 462.0 | 360.0 | 216.0 | 1.860 |
| 100814A | 1.44 | 0.093 | 344.0 \pm 32.0 | 8.200 | 0.491 | 0.444 | 60.8 | 589.0 | 164.0 | 170.0 | 167.0 | 0.920 |
| 110213A | 1.46 | 0.087 | 241.0 \pm 21.0 | 6.400 | 0.332 | 0.299 | 11.9 | 324.0 | 199.0 | 207.0 | 284.0 | 2.090 |
| 120922A | 3.1 | 0.167 | 156.0 \pm 26.0 | 20.000 | 0.234 | 0.261 | 44.5 | 891.0 | 190.0 | 138.0 | 398.0 | 2.900 |
| 130420A | 1.3 | 0.054 | 331.0 \pm 18.0 | 7.190 | 0.653 | 0.599 | 45.7 | 356.0 | 190.0 | 176.0 | 109.0 | 0.350 |
| 130612A | 2.01 | 0.172 | 186.0 \pm 32.0 | 0.716 | 0.488 | 0.443 | 1.9 | 110.0 | 246.0 | 219.0 | 212.0 | 0.875 |
| 130831A | 0.48 | 0.164 | 80.9 \pm 13.3 | 0.757 | 0.158 | 0.163 | 11.9 | 724.0 | 93.3 | 92.0 | 185.0 | 0.296 |
| 131231A | 0.64 | 0.042 | 288.0 \pm 12.0 | 20.000 | 0.288 | 0.299 | 17.7 | 100.0 | 240.0 | 237.0 | 239.0 | 1.700 |
| 140629A | 2.28 | 0.199 | 282.0 \pm 56.0 | 6.000 | 0.418 | 0.444 | 7.9 | 151.0 | 293.0 | 246.0 | 298.0 | 2.700 |
| $dE_{p,z}/E_{p,z} \gtrsim 0.2$ | | | | | | | | | | | | |
| 050922C | 2.2 | 0.266 | 417.0 \pm 111.0 | 4.530 | 0.773 | 0.739 | 2. | 132.0 | 401.0 | 408.0 | 619.0 | 19.000 |
| 060210 | 3.91 | 0.323 | 575.0 \pm 186.0 | 41.500 | 0.568 | 0.408 | 51.9 | 676.0 | 248.0 | 280.0 | 316.0 | 5.960 |
| 060418 | 1.49 | 0.250 | 571.0 \pm 143.0 | 12.800 | 0.832 | 0.738 | 41.4 | 151.0 | 244.0 | 255.0 | 187.0 | 1.890 |
| 060607A | 3.08 | 0.348 | 575.0 \pm 200.0 | 10.900 | 0.886 | 0.774 | 25. | 178.0 | 271.0 | 284.0 | 191.0 | 2.000 |
| 070110 | 2.35 | 0.460 | 370.0 \pm 170.0 | 5.500 | 0.618 | 0.200 | 26.4 | 1170.0 | 135.0 | 207.0 | 117.0 | 0.451 |
| 081007 | 0.53 | 0.246 | 61.0 \pm 15.0 | 0.170 | 0.178 | 1.090 | 6.5 | 123.0 | 152.0 | 77.1 | 85.8 | 0.043 |
| 091029 | 2.75 | 0.287 | 230.0 \pm 66.0 | 7.400 | 0.297 | 0.317 | 10.5 | 407.0 | 218.0 | 213.0 | 234.0 | 1.320 |
| 100906A | 1.73 | 0.348 | 158.0 \pm 55.0 | 33.400 | 0.220 | 1.220 | 33.1 | 100.0 | 396.0 | 160.0 | 366.0 | 2.450 |
| 130215A | 0.6 | 0.408 | 248.0 \pm 101.0 | 2.500 | 0.471 | 0.447 | 90. | 741.0 | 111.0 | 113.0 | 63.9 | 0.084 |
| 141109A | 2.93 | 0.404 | 750.0 \pm 303.0 | 31.000 | 0.891 | 0.150 | 23.5 | 955.0 | 193.0 | 376.0 | 240.0 | 4.200 |
| 141221A | 1.45 | 0.228 | 372.0 \pm 85.0 | 1.900 | 0.888 | 0.723 | 9.7 | 110.0 | 216.0 | 233.0 | 142.0 | 0.700 |
| $\epsilon_\gamma \gtrsim 50\%$ sub-sample (23 bursts) | | | | | | | | | | | | |
| GRB | z | $dE_{p,z}/E_{p,z}$ | $E_{p,z}$ (keV) | E_{iso} (10^{52} erg) | E_{ratio} | η/Γ | $T_{90,i}$ s | $T_{p,op}$ s | Γ_{op} | Γ_E | Γ_L | L_{iso} (10^{52} erg s $^{-1}$) |
| 990123 | 1.6 | 0.043 | 2030.0 \pm 88.0 | 239.000 | 1.700 | 1.150 | 23.9 | 47.9 | 656.0 | 677.0 | 417.0 | 35.300 |
| 060605 | 3.78 | 0.512 | 490.0 \pm 251.0 | 2.830 | 1.120 | 3.610 | 16.6 | 479.0 | 200.0 | 209.0 | 146.0 | 0.951 |
| 061121 | 1.31 | 0.093 | 1290.0 \pm 120.0 | 26.100 | 1.940 | 10.300 | 7.7 | 162.0 | 301.0 | 543.0 | 332.0 | 14.100 |
| 071112C | 0.82 | 0.546 | 597.0 \pm 326.0 | 1.600 | 1.760 | 1.950 | 2.9 | 178.0 | 187.0 | 333.0 | 89.8 | 0.400 |
| 080319B | 0.94 | 0.013 | 1260.0 \pm 17.0 | 150.000 | 1.050 | 0.134 | 23. | 17.4 | 810.0 | 508.0 | 281.0 | 9.590 |
| 080804 | 2.2 | 0.056 | 809.0 \pm 45.0 | 11.500 | 1.370 | 0.443 | 10.6 | 63.1 | 437.0 | 358.0 | 189.0 | 2.690 |
| 080810 | 3.35 | 0.121 | 1490.0 \pm 180.0 | 39.100 | 2.060 | 1.330 | 24.4 | 117.0 | 453.0 | 460.0 | 257.0 | 9.270 |
| 080916C | 4.35 | 0.089 | 2760.0 \pm 246.0 | 560.000 | 1.930 | 0.035 | 11.5 | 6.2 | 2060.0 | 1050.0 | 600.0 | 104.000 |
| 081203A | 2.1 | 1.200 | 1540.0 \pm 1854.0 | 35.000 | 2.240 | 3.020 | 96.4 | 309.0 | 274.0 | 327.0 | 146.0 | 2.810 |
| 090323 | 3.57 | 0.108 | 1900.0 \pm 206.0 | 390.000 | 1.320 | 3.580 | 29.1 | 200.0 | 504.0 | 663.0 | 446.0 | 38.500 |
| 090812 | 2.45 | 0.449 | 2020.0 \pm 908.0 | 40.300 | 3.060 | 0.496 | 9.5 | 47.9 | 583.0 | 681.0 | 229.0 | 9.550 |
| 090902B | 1.82 | 0.015 | 2020.0 \pm 31.0 | 440.000 | 1.380 | 0.094 | 6.9 | 8.5 | 1390.0 | 994.0 | 529.0 | 58.900 |
| 100414A | 1.39 | 0.020 | 1490.0 \pm 29.0 | 76.900 | 1.640 | 0.281 | 9.2 | 34.7 | 622.0 | 638.0 | 226.0 | 7.000 |
| 110731 | 2.83 | 0.057 | 1210.0 \pm 69.0 | 40.000 | 1.550 | 0.041 | 1.75 | 5.0 | 1410.0 | 805.0 | 459.0 | 27.000 |
| 120711A | 1.4 | 0.039 | 2340.0 \pm 91.0 | 150.000 | 2.400 | 7.910 | 17.2 | 240.0 | 328.0 | 744.0 | 266.0 | 15.200 |
| 120909A | 3.93 | 0.067 | 1820.0 \pm 123.0 | 72.900 | 2.190 | 2.400 | 23.3 | 288.0 | 366.0 | 557.0 | 210.0 | 7.190 |
| 130427A | 0.34 | 0.009 | 1380.0 \pm 13.0 | 80.900 | 1.450 | 1.260 | 46.1 | 21.9 | 599.0 | 413.0 | 435.0 | 27.000 |
| 130610A | 2.09 | 0.419 | 912.0 \pm 382.0 | 6.810 | 1.920 | 3.150 | 7. | 204.0 | 260.0 | 395.0 | 171.0 | 2.400 |
| 160629A | 3.33 | 0.074 | 1280.0 \pm 95.0 | 47.000 | 1.580 | 0.688 | 14.9 | 81.3 | 531.0 | 494.0 | 272.0 | 9.100 |
| 061007 | 1.26 | 0.030 | 902.0 \pm 27.0 | 88.100 | 0.804 ^a | 2.220 | 25.5 | 74.1 | 466.0 | 392.0 | 427.0 | 17.400 |
| 110205A | 2.22 | 0.335 | 714.0 \pm 239.0 | 56.000 | 0.685 ^a | 8.540 | 79.8 | 813.0 | 205.0 | 248.0 | 193.0 | 2.500 |
| 121128A | 2.2 | 0.050 | 198.0 \pm 10.0 | 14.000 | 0.197 ^a | 1.220 | 3.1 | 74.1 | 422.0 | 247.0 | 516.0 | 6.400 |
| 140423A | 3.26 | 0.122 | 533.0 \pm 65.0 | 56.000 | 0.464 ^a | 1.550 | 22.3 | 200.0 | 385.0 | 294.0 | 319.0 | 5.660 |

^a $\epsilon_\gamma \gtrsim 50\%$ judged from E_{iso}/E_k .

TABLE 7
THE OBSERVED QUANTITIES AND THE PROPERTIES OF $E_{\text{iso}}/L_{X,11}$ FOR THE BURSTS WITH MAXIMUM Γ .

| GRB | z | $T_{90,i}$ s | $dE_{p,z}/E_{p,z}$ | E_{ratio} | $E_{p,z}$ (keV) | E_{iso} (10^{52} erg) | $L_{X,11}$ (10^{45} erg s $^{-1}$) | $E_{\text{iso}}/L_{X,11}$ | $T_{p,op}$ s | Γ_{op} | $\Gamma_{op}/\Gamma_{\text{max}}$ | L_{iso} (10^{52} erg s $^{-1}$) |
|---------|------|-----------------|--------------------|--------------------|--------------------|--------------------------------------|---|---------------------------|-----------------|---------------|-----------------------------------|---|
| 100414A | 1.39 | 9.2 | 0.020 | 1.640 | 1490.0 ± 29.0 | 76.900 | | | 34.7 | 622.0 | 1.040 | 7.000 |
| 090812 | 2.45 | 9.5 | 0.449 | 3.060 | 2020.0 ± 908.0 | 27.18 | 6.525 | 4.166 | 47.9 | 583.0 | 0.902 | 9.550 |
| 160629A | 3.33 | 14.9 | 0.074 | 1.580 | 1280.0 ± 95.0 | 47.000 | | | 81.3 | 531.0 | 0.832 | 9.100 |
| 100728B | 2.11 | 3.9 | 0.116 | 1.000 | 404.0 ± 47.0 | 2.66 | 0.841 | 3.163 | 33.9 | 462.0 | 1.076 | 1.860 |
| 050502A | 3.79 | | | 1.025 | 498.9 | 3.981 | | | 57.5 | 461.4 | 0.989 | 2.600 |
| 080804 | 2.2 | 10.6 | 0.056 | 1.370 | 809.0 ± 45.0 | 11.500 | 3.181 | 3.615 | 63.1 | 437.0 | 0.928 | 2.690 |
| 081008 | 1.97 | | | 0.438 | 267.3 | 4.19 | 0.915 | 4.579 | 162.2 | 261.5 | 0.961 | 0.300 |
| 080310 | 2.42 | | | 0.087 | 75.0 | 3.25 | 1.78 | | 182.0 | 255.8 | 0.881 | 0.390 |
| | | | | | | | | | (2000) | (104) | (0.352) | |
| 081007 | 0.53 | 6.5 | 0.246 | 0.178 | 61.0 ± 15.0 | 0.170 | | | 123.0 | 152.0 | 0.908 | 0.043 |

TABLE 8
THE OBSERVED QUANTITIES, INFERRED EFFICIENCY, AND THE PROPERTIES OF EXTENDED EMISSION FOR THE SHORT GRBs.

| $\epsilon_{\gamma} \lesssim 50\%$ sub-sample (8 bursts) | | | | | | | | | | | |
|---|---------|---------------------------|---|---|---|-------------------------------------|---|---------------------------------|--|--------------------------------|--|
| GRB | z | $E_{p,z}$ (keV) | E_{iso} (10^{52} erg) | $L_{X,11}$ (10^{45} erg s $^{-1}$) | $E_{\text{iso}}/[\frac{3.7 * L_{X,11}}{(1+z)^2}]$ | E_{ratio} | $T_{90,i}$ s | | | | |
| 051221A | 0.5465 | $677.0^{+200.0}_{-141.0}$ | 0.91 | 0.277 | 0.687 | 0.296 | 0.14 | | | | |
| 070724A | 0.457 | 119.5 ± 7.3 | 0.0016 | 0.0271 | 0.0116 | 0.243 | 0.27 | | | | |
| 070809 | 2.187 | 464.0 ± 223.0 | 0.104 | 0.338 | 0.133 | 0.368 | 0.44 | | | | |
| 130603B | 0.356 | $823.0^{+83.0}_{-71.0}$ | 0.196 | 0.0773 | 0.465 | 0.64 | 0.16 | | | | |
| 131004A | 0.71 | 202.0 ± 51.0 | 0.068 | 0.145 | 0.109 | 0.14 | 0.9 | | | | |
| 140903A | 0.351 | 60.0 ± 22.0 | 0.0044 | 0.285 | 0.00281 | 0.0691 | 0.22 | | | | |
| 150423A | 0.22 | 146.0 ± 43.0 | 0.00075 | 0.0701 | 0.00176 | 0.408 | 1.14 | | | | |
| 160821B | 0.16 | 97.4 ± 22.0 | 0.012 | 0.0115 | 0.164 | 0.0944 | 0.41 | | | | |
| $\epsilon_{\gamma} \gtrsim 50\%$ sub-sample (4 bursts) | | | | | | | | | | | |
| GRB | z | $T_{90,i}$ s | $L_{X,11}$ (10^{45} erg s $^{-1}$) | $E_{\text{iso}}/[\frac{3.7 * L_{X,11}}{(1+z)^2}]$ | E_{iso} (10^{52} erg) | $E_{p,z}$ (keV) | $E_{\text{iso}}^{\text{Ext}}$ (10^{52} erg) | $E_{p,z}^{\text{Ext}}$ (keV) | $E_{\text{iso}}/E_{\text{iso}}^{\text{Ext}}$ | $E_{p,z}/E_{p,z}^{\text{Ext}}$ | |
| 070714B | 0.923 | 0.65 | 0.040 | 4.127 | 0.640 | 1060^{+285}_{-215} | 0.116 | 164.87 ± 73.13 | 5.517 | 6.429 | |
| 110402A | 0.805 | 2.8 | 0.255 | 1.454 | 1.520 | 1924^{+767}_{-451} | 0.642 | | | | |
| 150424A | 0.30 | 0.21 | 0.177 | 0.431 | 0.434 | 1191^{+94}_{-61} | 0.0625 | 82.3 ± 82.1 | 6.944 | 14.349 | |
| 160410A | 1.717 | 0.58 | 0.441 | 7.749 | 9.300 | 3853^{+1429}_{-973} | 1.55 | 495.3 ± 232.9 | 6.000 | 7.779 | |
| 170817A | 0.00968 | 0.50 | | | $(4.7 \pm 0.7) \times 10^{-6}$ | $65.6^{+35.3}_{-14.1}$ | $(1.6 \pm 0.2) \times 10^{-6}$ | 38.4 ± 4.2 | 3 | 1.708 | |
| 061006A | 0.4377 | 0.26 | | | 0.382 | 909^{+260}_{-191} | 0.0674 | 150 | 5.668 | 6.060 | |
| 071227A | 0.384 | 1.30 | | | 0.0591 | 875^{+790}_{-287} | 0.0196 | 80 | 3.015 | 10.938 | |
| 080123A | 0.495 | 0.27 | | | 0.32 | 2228^{+1272}_{-1308} | 0.0398 | 53 | 8.040 | 42.038 | |
| 061210A | 0.4095 | 0.07 | | | 0.0024 | 761^{+648}_{-264} | 0.0422 | | | | |
| 060614A | 0.1254 | 4.4 | | | 0.24 | 340^{+241}_{-96} | 0.0765 | | | | |
| 050709A | 0.1606 | 0.06 | | | 0.0027 | $96.3^{+20.9}_{-13.9}$ ^a | | | | | |
| 050724A | 0.2576 | 2.4 | | | 0.009 | 138^{+503}_{-57} ^a | | | | | |

^a Only detected by *Swift* or HETE-2 (lacking detections in the high-energy band).